Monthly Notices
of the
ROYAL ASTRONOMICAL SOCIETY

MNRAS **469,** 2771–2790 (2017)
Advance Access publication 2017 March 24

doi:10.1093/mnras/stx163

Photometric redshifts and clustering of emission line galaxies selected jointly by DES and eBOSS

S. Jouvel,[1]★ T. Delubac,[2] J. Comparat,[3,4]† H. Camacho,[5,6] A. Carnero,[6,7] F. B. Abdalla,[1,8] J.-P. Kneib,[2] A. Merson,[1] M. Lima,[5,6] F. Sobreira,[6,9] Luiz da Costa,[6,7] F. Prada,[3,10,11,12] G. B. Zhu,[13]‡ A. Benoit-Levy,[1] A. De La Macora,[14] N. Kuropatkin,[9] H. Lin,[9] T. M. C. Abbott,[15] S. Allam,[9] M. Banerji,[16,17] E. Bertin,[18,19] D. Brooks,[1] D. Capozzi,[20] M. Carrasco Kind,[21,22] J. Carretero,[23,24] F. J. Castander,[23] C. E. Cunha,[25] S. Desai,[26,27] P. Doel,[1] T. F. Eifler,[28,29] J. Estrada,[9] A. Fausti Neto,[6] B. Flaugher,[9] P. Fosalba,[23] J. Frieman,[9,30] E. Gaztanaga,[23] D. W. Gerdes,[31] D. Gruen,[32,33] R. A. Gruendl,[21,22] G. Gutierrez,[9] K. Honscheid,[34,35] D. J. James,[15] K. Kuehn,[36] O. Lahav,[1] T. S. Li,[37] M. A. G. Maia,[6,7] M. March,[28] J. L. Marshall,[37] R. Miquel,[24,38] R. Ogando,[7] W. J. Percival,[20] A. A. Plazas,[29] K. Reil,[39] A. K. Romer,[40] A. Roodman,[25,40] E. S. Rykoff,[25,40] M. Sako,[28] E. Sanchez,[41] B. Santiago,[6,42] V. Scarpine,[9] I. Sevilla-Noarbe,[21,41] M. Soares-Santos,[9] E. Suchyta,[34,43] G. Tarle,[31] J. Thaler,[44] D. Thomas,[20] A. Walker,[15] Y. Zhang[31] and J. Brownstein[45]

Affiliations are listed at the end of the paper

Accepted 2017 January 16. Received 2017 January 16; in original form 2015 September 25

ABSTRACT

We present the results of the first observations of the emission line galaxies (ELG) of the extended Baryon Oscillation Spectroscopic Survey. From the total 9000 targets, 4600 have been selected from the Dark Energy Survey (DES). In this subsample, the total success rate for redshifts between 0.6 and 1.2 is 71 and 68 per cent for a bright and a faint samples, respectively, including redshifts measured from a single strong emission line. The mean redshift is 0.80 for the bright and 0.87 for the faint sample, while the percentage of unknown redshifts is 15 and 13 per cent, respectively. In both cases, the star contamination is lower than 2 per cent. We evaluate how well the ELG redshifts are measured using the target selection photometry and validating with the spectroscopic redshifts measured by eBOSS. We explore different techniques to reduce the photometric redshift outliers fraction with a comparison between the template fitting, the neural networks and the random forest methods. Finally, we study the clustering properties of the DES SVA1 ELG samples. We select only the most secure spectroscopic redshift in the redshift range $0.6 < z < 1.2$, leading to a mean redshift for the bright and faint sample of 0.85 and 0.90, respectively. We measure the projected angular correlation function and obtain a galaxy bias averaging on scales from 1 to 10 Mpc h^{-1} of 1.58 ± 0.10 for the bright sample and 1.65 ± 0.12 for the faint sample. These values are representative of a galaxy population with $M_B - \log(h) < -20.5$, in agreement with what we measure by fitting galaxy templates to the photometric data.

Key words: surveys – cosmology: observations.

1 INTRODUCTION

With the development of new technologies and instruments, we can now design wider and deeper surveys with performances several

★ E-mail: s.jouvel@ucl.ac.uk
† Severo Ochoa IFT Fellow.
‡ Hubble Fellow.

orders of magnitudes greater than 20 yr ago. Classically, these surveys fall into two categories: spectroscopic and photometric redshift surveys. Both have advantages and disadvantages and they mutually benefit from each other. Some observables are only accessible with one design, for example, weak lensing can only be measured with photometric data, likewise, spectroscopic surveys need photometric catalogues to create the target selection and photometric surveys need spectroscopic surveys to obtain distances. Both aspects are subjects of this paper.

The Dark Energy Spectroscopic Instrument (DESI, Schlegel et al. 2011) and the extended Baryon Oscillation Spectroscopic Survey (eBOSS)[1] (Dawson et al. 2016) are a new generation of surveys using the latest technologies in the field of spectroscopy. Using these new instruments allow to cover large sky areas selecting higher redshift and fainter targets than previous surveys, increasing the statistical confidence in the measurement of cosmological parameters.

One of the galaxy targets of these surveys are emission line galaxies (ELG). Previously, several papers have studied the survey design needed to target ELGs, such as Comparat et al. (2013); Adelberger et al. (2004), and efficient ELG samples have been compiled by the Deep Extragalactic Evolutionary Probe 2 (DEEP2, Newman et al. 2013), the VIMOS Public Extragalactic Redshift Survey (VIPERS, Garilli et al. 2014) and The Wigglez Dark Energy Survey (DES, Parkinson et al. 2012).

None the less, in order to further optimize the selection efficiency, different techniques have been studied. Abdalla et al. (2008) showed that a neural network can pick up strong emission lines from the broad-band photometry of DEEP2 and the Sloan Digital Sky Survey (SDSS) data release of Abazajian et al. (2004). This optimization method was later applied to a DESI-like survey in Jouvel et al. (2014a). They find that one can reach a higher success rate if targets are picked using a neural network algorithm, rather than the classical selection in colour space. Likewise, a related work uses a Fisher discriminant method to investigate improvements in the eBOSS target selections (Raichoor et al. 2016).

On the photometric side, one of the main limitations in ongoing and upcoming photometric surveys is the access to the radial dimension, the redshift (Newman et al. 2015). Surveys such as the Dark Energy Survey[2], the Large Synoptic Survey Telescope (Ivezic et al. 2008), *Euclid* (Laureijs et al. 2011), use between 4 and 8 photometric broad-bands. Broad-band photometric redshifts (z_{ph}) have an accuracy limited by the filter resolution (Jouvel et al. 2011). In the optimal case of a space-based survey with 16 filters, covering from UV to infrared, photometric redshifts reach a mean precision of 0.03 (Jouvel et al. 2014b). Depending on the survey configuration such as ground-based or space-based, number of broad-band filters, pixel size and exposure time, the photometric redshifts accuracy will vary. For example, DES will reach a precision of 0.08 (Sánchez et al. 2014), which will vary, depending on the galaxy population considered.

If photometric redshifts are used to measure galaxy clustering, then the resulting estimate of the dark matter power spectrum becomes biased because the density fluctuation traced by galaxies is smoothed by the photometric redshift error. The bluest galaxies have higher degeneracies in colour space, which misplace high-redshift galaxies at low redshift, and conversely. Dark Energy Equation of State constraints, which rely on photometric redshift information (like weak-lensing and cluster mass function estimates) is severely affected by (unaccounted) outliers (Bernstein & Huterer 2010).

In this paper, we present the characteristics of the emission line galaxy samples observed with eBOSS. We designed different target selections based on SDSS (Ahn et al. 2014), the South Galactic Cap *u*-band Sky Survey (SCUSS, Jia et al. 2014) and DES. These data are part of the eBOSS ELG target selection definition effort, undergone in 2014 October. In particular, we focus our attention in the study of the target selection defined with DES only.

We investigate the precision of DES to measure ELG redshifts, and study possible ways to reduce the outliers fraction. Finally, we measure the clustering properties of the spectroscopically confirmed ELGs, assessing the properties of the galaxy population, based on two different target selection proposals.

In Section 2, we present the ELG target selections based on DES data. In Section 3, we use the eBOSS spectroscopic redshifts to test DES photometric redshifts and study the outliers fraction. In Section 4, we study the clustering properties of the spectroscopic samples. Finally, we present the conclusions in Section 5.

We highlight two companion papers: Comparat et al. (2016), which explains the observation strategy and the automated redshift assignment in ELGs and Delubac et al. (2017), which studies the SDSS-based photometric target selections.

2 THE eBOSS ELG SAMPLE FROM DES PHOTOMETRY

2.1 eBOSS ELG survey strategy

eBOSS is a spectroscopic survey using the BOSS spectrograph (Smee et al. 2013) at the Apache Point Observatory. It will cover 7500 deg^2 in a 6-yr period. eBOSS aims at measuring the baryon acoustic oscillation features at redshift higher than 0.6, extending the first measurement from SDSS at lower redshift (Percival et al. 2010). eBOSS will use a mixture of targets to have a measurement at $z \sim 0.6$ using luminous red galaxies (LRG), $z \sim 1$ using ELG, quasars between redshift one and two (Leistedt & Peiris 2014), and Lyα absorption quasars at redshift higher than two (Font-Ribera et al. 2014). The LRG and quasars survey started in 2014 July while the ELG survey will start in 2016 and cover 1500 deg^2 only with a higher density of targets. The eBOSS ELG survey plans to use the DECaLS[3] photometry to select its targets on $\sim$1000 deg^2. In this paper, we use DES photometry to look at possible optimization of the target selection: reach fainter targets at higher redshift and lower contamination from low redshift galaxies. This paper investigates the target density, redshift range from the DES SVA1-eBOSS observations and systematics from a DES target selection based on year one data. We study the systematics of using DES year one data since the quality of the data reduction is higher than in SVA1. SVA1 data were taken for quality tests and calibration purposes (see Figs 2 and 5).

2.2 Des science verification data

DES is an ongoing photometric ground-based galaxy survey that started in autumn 2013. DES uses the brand new 2.2 deg^2 DECam instrument (Flaugher et al. 2015) mounted on the 4 m Victor M.

[1] https://www.sdss3.org/future/eboss.php
[2] http://www.darkenergysurvey.org/
[3] legacysurvey.org

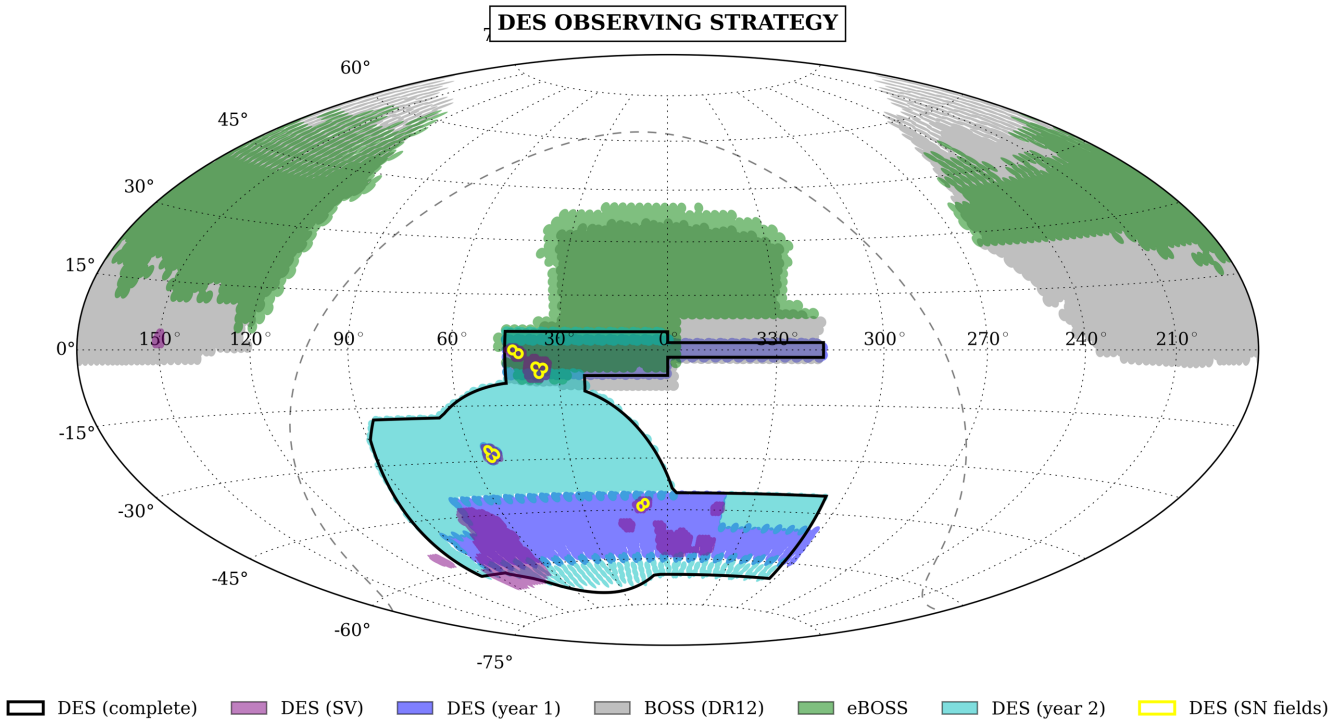

Figure 1. Footprints of DES, BOSS and eBOSS. Coordinates are RA and Dec in deg.

Blanco Telescope located at the Cerro Tololo Inter-American Observatory (CTIO) in Chile. It will cover 5000 deg^2 after completion in five optical broad-bands observing the southern sky. DES will use cosmic shear, cluster counts, large-scale structure measurements and supernovae type Ia to reach very competitive measurement of the Universe growth rate and dark energy.

The first phase of the DES survey consisted of various tests and improvements in the data acquisition, instrument calibration and data processing, which resulted in a first well-defined source catalogue, the Science verification data, hereafter SVA1. Scientific results from Bonnett et al. (2016); Rozo et al. (2016); Crocce et al. (2016); Banerji et al. (2015); Sánchez et al. (2014); Melchior et al. (2016); Dark Energy Survey Collaboration et al. (2016) and others show the very good quality of the SVA1 data. In Fig. 1, we show the footprint of the DES, BOSS and eBOSS surveys along with the DES year one data, and the SVA1 data.

2.3 Photometric redshift of DES SVA1

Sánchez et al. (2014) studied the photometric redshift of SVA1 galaxies. In our paper, we use two of the codes presented in this paper: ANNZ2 (Sadeh, Abdalla & Lahav 2016) and LE PHARE (Ilbert et al. 2006, 2009). ANNZ2 is a machine learning code that includes several algorithms: neural networks, boosted decision trees and k-nearest neighbours, while LE PHARE is a template fitting method. Both produce single point estimates, as well as probability distributions for their photometric redshifts. ANNZ2 also includes a weighting algorithm during the training procedure, taking into account the differences in magnitude, colours and redshifts between the photometric and spectroscopic sample (Lima et al. 2008). In Sánchez et al. (2014), the spectroscopic sample used to train and validate photometric redshifts contains 9000 spectroscopic redshifts (z_{sp}) from various spectroscopic surveys compiled from the literature. We also use the same set-up to train and obtain the ELG redshifts. We highlight that eBOSS redshifts are not included in the spectroscopic redshifts used to train our data.

For ANNZ2, we actually use the photo-z estimates presented in Sánchez et al. (2014), while for LE PHARE, the set up is identical, but with different zero-point calibrations. In our case, we compute zero-point corrections independently for the ELG sample and apply them to the LE PHARE template fitting procedure. The template library used, both in Sánchez et al. (2014) and here, is the template library developed for the COSMOS observations (Ilbert et al. 2009). It has 31 templates, from elliptical to starburst galaxies. We allow for internal extinction for the bluest templates, using the Calzetti law (Calzetti et al. 2000) with extinction values of $E(B-V) = [0.1, 0.2, 0.3]$. We also use a redshift prior that is calibrated with the Vimos VLT Deep Survey (VVDS) observations (Le Fèvre et al. 2005). DES observations have the same depth as VVDS that justify the use of this prior.

2.4 eBOSS ELG spectroscopic targets

To define the target selection of the eBOSS ELG sample, we used an area of 9.2 deg^2 from the SVA1 data, overlapping with eBOSS. Fig. 2 shows the depth over the 9.2 deg^2 SVA1 footprint in g,r,z used for the eBOSS observations. Limiting magnitudes are defined by the flux in a 2 arcsec aperture above 10σ, computed from the DES images using the MANGLE software (Swanson et al. 2012) (Appendix B).

The eBOSS fields selected for the ELG target selection campaign were chosen to overlap with Canada-France-Hawaii Telescope Legacy Survey W1 field (CFHTLS-W1). CFHTLS has four wide and four deep 1 deg^2 fields in u^*,g',r',i',z' bands. The W1 field is the biggest of the wide fields with 72 deg^2 and 80 per cent completeness depth of $i' < 24.5$. Coupon et al. (2009) computed the CFHTLS photometric redshift accurate to 3–4 per cent up to $i' < 22.5$ calibrated with VVDS (Le Fèvre et al. 2005), DEEP2 (Newman et al. 2013) and zCOSMOS (Lilly et al. 2007)

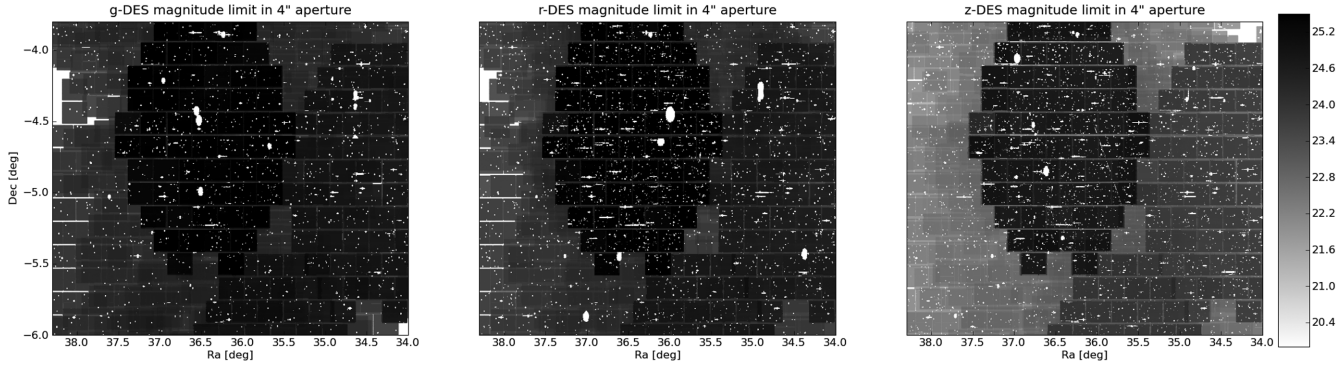

Figure 2. Depth of the g,r,z bands of the DES Science Verification data in the 9.2 deg^2 of the eBOSS observations. The depth has been computed with the MANGLE software and corresponds to a 10σ magnitude in an aperture of 2 arcsec; see Appendix B.

Table 1. The three eBOSS ELG selections. The SDSS-SCUSS selection is a mix of two different selections. We use an SDSS only selection with g,r,z bands and an SDSS-SCUSS selection using the u band from the SCUSS survey and g,r,z bands from SDSS. eg, er, ei, ez are photometric uncertainties of the g,r,i,z bands. Magnitudes are the SExtractor (Bertin & Arnouts 1996) detmodel DES magnitudes for the bright and faint selections and SDSS/SCUSS model magnitudes for the SDSS-SCUSS selections. The different elements of a selection in a column are connected by the logical operator 'and'. SExtractor parameters are defined in Appendix A.

DES bright	DES faint	SDSS-SCUSS	
$20.5 < g < 22.8$	$g > 20.45$	$eg < 0.6$ & $er < 1$ & $ei < 0.4$	
$-0.7 < g - r < 0.9$	$r < 22.8$	$20 < g < 23$	$21 < g < 22.5$
$0 < r - z < 2$	$0.28 < r - z < 1.58$	$r < 22.5$	$r < 22.5$
$r - z > 0.4*(g - r) + 0.4$	$g - r < 1.15*(r - z) - 0.2$	$i < 21.6$	$i < 21.6$
	$g - r < 1.45 - 1.15*(r - z)$	$21 < U < 22.5$	$g - r < 0.8$
		$r - i > 0.7$	$r - i > 0.8$
		$i - u > -3.5*(r - i) + 0.7$	

spectroscopic surveys. These data are publicly available. This field has also been imaged by the SDSS survey.[4] The photometry from SDSS is a 11k deg^2 with 95 per cent completeness depth of u, g, r, i, $z = 22.0, 22.2, 22.2, 21.3, 20.5$ (Abazajian et al. 2009).

We used three tiles from the SVA1 data on CFHTLS-W1 that we observed in eight eBOSS plates. With a 1 h exposure we reached a total of 5705 spectra. We investigated three different target selection schemes, see Table 1.

SDSS-SCUSS represent two distinct target selections, one using SDSS data alone and another combining SDSS with SCUSS photometry (Table 1). These targets are distributed over 51 deg^2. DES bright and faint targets are distributed over 9.2 deg^2. The DES faint selection has been optimized to reach redshifts between 0.7 and 1.5. This latter selection has been designed for the DESI survey and reaches higher redshifts galaxies than eBOSS is aiming at (Schlegel et al. 2011). eBOSS is aiming at galaxies between a redshift of 0.6 and 1.2. Higher redshifts will be explored using AGNs. This papers studies the DES ELG target selections for eBOSS. The two other selections using SDSS and SCUSS data will be presented in our companion papers: Comparat et al. (2016), Delubac et al. (2017) and Raichoor et al. (2016). On the DES selections, we do not apply any star–galaxy separation. We do not expect much contamination by stars when designing ELG target selection as shown in Adelberger et al. (2004). We remove the fake detections by applying selection criteria in g,r,z DES bands of $MAG\_APER - MAG\_DETMODEL < 2$, see Appendix A for parameters explanations.

[4] http://www.sdss.org/data

Right-hand panel of Fig. 3 shows the photometric redshifts distribution in cyan solid line of the DES SVA1 galaxies in the 9.2 deg^2 field used to optimize the eBOSS target selections. The cyan solid line shows all galaxies at $g < 23$ with a photometric redshift between 0.5 and 1.5. We show two of the DES based target selections in dash–dotted blue and dashed green lines. The red dotted line shows the SDSS-based selection that we name SDSS-SCUSS, detailed in the next section. The magenta triangles show the outliers. We note that there is colour space where there seem to be a higher percentage of outliers, especially for the DESI selection. In Section 3.3, we present a first attempt to identify regions in colour–colour space with a higher percentage of outliers.

2.5 eBOSS ELG spectroscopic results

The eBOSS ELG observations are presented in Table 2. We show the number of targets selected and observed in the eBOSS observations. SDSS-SCUSS do not show the total number of targets observed but the one for which we find a match with DES photometry. For representative statistics about the SDSS and SCUSS selections, please refer to Comparat et al. (2016), Delubac et al. (2017) and Raichoor et al. (2016). We show the percentage of spectroscopic redshifts with a secure redshift 'secure' for which we find at least two lines with a low signal-to-noise detection, or one line and a 10σ continuum detection for the redshift measurement. The '1line' were measured from a single line with at least 3σ detection without continuum information. They have a higher failure rate since a line confusion can happen between [$H\alpha$] and [O II]. The 'unknown' are spectra for which we could not find a redshift. '$0.6 < z < 1.2$' shows the percentage of targets with secure redshifts in the desired

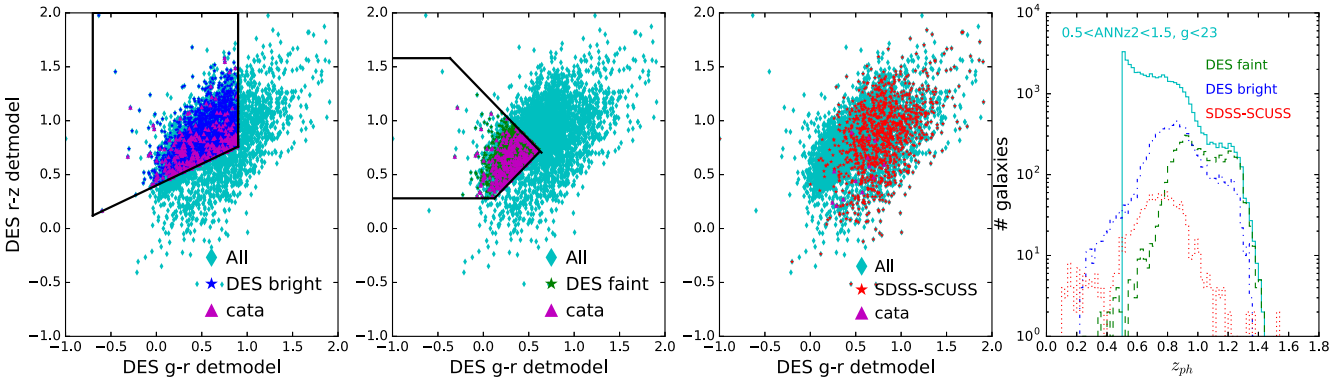

Figure 3. From the left, the first two panels show the two DES-based ELG selections while the third panel shows an SDSS-SCUSS-based ELG selection using the eBOSS observations. The magenta triangles labelled 'cata' show catastrophic redshifts as defined in Section 3. The furthest right-hand panel shows the photometric redshift distribution of the eBOSS targets selected with the DES SVA1. Photo-z for the DES SVA1 data are computed using ANNZ2. For SDSS-SCUSS selection, we used CFHTLS photo-z, which we matched with SDSS photometry. The median uncertainties on $g-r$ and $r-z$ colours for the different selections are less than 4 per cent.

Table 2. Number of targets, efficiency and spectroscopic success rate for the three eBOSS selections. The last column shows the overlap between the DES bright and faint selections. Note that the magnitude selections are carried out in the DES g band.

Magnitude selection		DES bright	DES faint	SDSS-SCUSS	DES bright∩faint
	Selected	953	445	–	220
	Dens. selected (deg^2)	69	32	–	24
	Observed	557	254	206	199
	Secure (per cent)	88.0	85.0	77.2	87.4
	1line (per cent)	1.3	3.5	1.0	2.5
$20.5 < g < 22$	Unknown (per cent)	10.8	11.4	21.8	10.1
	$0.6 < z < 1.2$(per cent)	60.9	66.5	58.3	71.4
	$0.6 < z < 1.2*$(per cent)	61.4	67.7	58.3	72.4
	$\bar{z}$	0.68	0.8	0.65	0.8
	$\langle$[O II]$\rangle$	1.8	2.54	3.91	2.65
	Nstars	21	13	25	5
	Selected	6762	7838	–	2158
	Dens. selected (deg^2)	491	570	–	239
	Observed	3103	2158	1049	1274
	Secure (per cent)	70.6	64.0	74.5	67.1
	1line (per cent)	13.4	22.3	4.6	21.3
$22 < g < 23$	Unknown (per cent)	16.0	13.6	21.0	11.6
	$0.6 < z < 1.2$(per cent)	64.8	55.7	62.7	60.4
	$0.6 < z < 1.2*$(per cent)	73.5	68.1	66.0	72.0
	$\bar{z}$	0.83	0.88	0.71	0.9
	$\langle$[O II]$\rangle$	1.24	1.47	0.97	1.71
	Nstars	51	35	24	16
	Selected	7716	8283	–	2378
	Dens. selected (deg^2)	561	602	–	264
	Observed	3660	2412	1255	1473
	Secure (per cent)	73.3	66.3	74.9	69.9
	1line (per cent)	11.6	20.4	4	18.7
$20.5 < g < 23$	Unknown (per cent)	15.2	13.4	21.1	11.4
	$0.6 < z < 1.2$ (per cent)	64.2	56.8	62	61.8
	$0.6 < z < 1.2*$(per cent)	71.6	68.0	64.7	72.0
	$\bar{z}$	0.8	0.87	0.7	0.88
	$\langle$[O II]$\rangle$	1.34	1.61	1.47	1.87
	Nstars	72	48	49	21

redshift range: $0.6 < z < 1.2$. '$0.6 < z < 1.2*$' includes the '1line' z_{sp} in the percentage of targets with secure redshifts. $\bar{z}$ and $\langle$[O II]$\rangle$ are respectively the mean eBOSS z_{sp} and [O II] flux using secure redshifts. Nstars is the number of stars. Comparat et al. (2016) gives a full detailed study of the eBOSS redshift measurement pipeline and finds an agreement with VIPERS at less than 1 per cent. We conclude that eBOSS redshift measurement are very reliable.

The highest success rate is achieved by the DES bright selection with 72 per cent of very secure redshift, 12 per cent of one line detected redshift and 15 per cent of non-identified redshift. DES

faint selection has a slightly lower success rate of 68 per cent of very secure redshifts including 20 per cent of one line z_{sp}. Table 2 shows the success rate as a function of DES g-band magnitude. The DES faint selection has been designed to target fainter and higher redshift galaxies that explains the slightly lower success rate when compared to DES bright selection. In Section 2.6, we apply the DES bright selection to the year one DES data and show the results of our systematics studies.

2.6 eBOSS ELG systematics

DES and eBOSS footprint have an overlap of 500 deg^2 in the Stripe82 region. The 500 deg^2 of DES targets will yield a minimum number of 60 000 eBOSS spectra over Stripe82. The early release of the DES year one data, hereafter Y1A1, is on Stripe82 with 152 deg^2. We use Y1A1 data to look at possible systematics from the photometric target selections. In order to have reliable measurement of the galaxy power spectrum, eBOSS needs to have a density variation lower than 15 per cent over the survey area as discussed in Ross et al. (2012) and Dawson et al. (2016). We use HEALPIX[5] to produce maps of the eBOSS galaxy target selection and survey variables that have the biggest impact on the power spectrum measurement such as stellar density, Galactic extinction, survey depth, airmass (Ross et al. 2012). We used the DES bright selection for the galaxy density maps using a pixelization of 6.87 arcmin^2 (NSIDE = 512). The mean number density of DES bright galaxies is 737 gal deg^{-2} with variations between 19 and 2690 gal deg^{-2}. In Fig. 4, we show the galaxy density fluctuation as a function of the stellar density using criteria defined in Section 2.2. We are aiming to look for possible correlations between variation in the stellar density and variation in the density of galaxies in the eBOSS bright selection. The number density of stars varies between 76 and 15 000 with a mean of 5890 stars deg^{-2}.

We compute the Spearman correlation coefficient, which is the correlation of the Pearson's coefficient between two ranked variables. Pearson's coefficient is a measure of the linear correlation of two variables. We choose to show the Spearman coefficient since it is more robust to outliers. We note that the Pearson and Spearman's coefficients give very similar results on our data. Spearman's coefficient vary between −1 and 1, which mean a very high correlation. A value of zero means no correlation between two variables. We find a value of 0.31 to Spearman's correlation between the stellar density and the galaxy density in the version of the DES data we are using (Y1A1-copper). This is a non-negligible correlation. We expect this correlation to decrease in future data releases and do not investigate this further at the present time.

Similarly, in Fig. D1, we looked at the variation of target density as a function of depth, Galactic extinction and airmass across the Y1A1 Stripe82. The depth map in g,r,z, bands of Y1A1 data is shown in Fig. 5. For the g,r,z depth, we find values of −0.04, 0.01, 0.07 for the Spearman's coefficients. For airmass in g,r,z bands, we find values of −0.03, −0.09, −0.03 for the Spearman's coefficients. For the Galactic extinction in g,r,z bands, we find a value of 0.1. There are no obvious correlations between the densities of DES bright galaxies and airmass, Galactic extinction or depth. We conclude that our Y1A1 target selection will be within requirement across the Stripe82 DES footprint.

[5] http://healpy.readthedocs.org/en/latest/

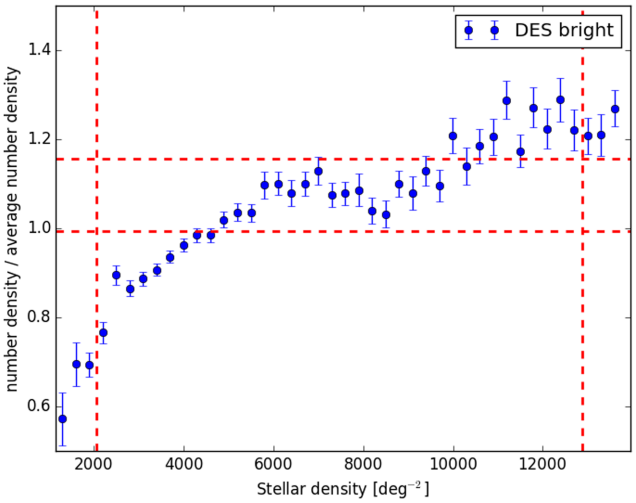

Figure 4. Density fluctuation of galaxies as a function of the stellar surface density. The two vertical red lines show the 5 and 95 per cent of the star density distribution. The two vertical red lines show the 15 per cent range around the error weighted mean galaxy density fluctuation for the eBOSS target selection. The error weighted mean galaxy density fluctuation is computed using 96 per cent of the galaxy population. We discarded a 2 per cent from the extremes low- and high-density fluctuations. Errorbars show the standard deviation of the galaxy number density over the HEALPIX pixels that we used as weight in the mean calculation.

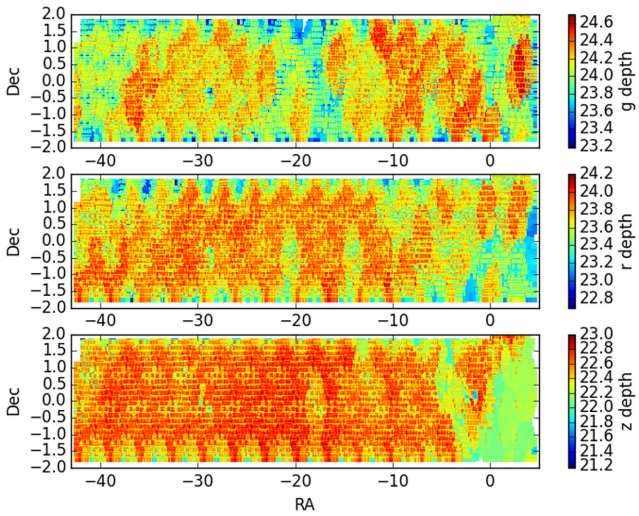

Figure 5. Depth of the DES year one data on Stripe 82 region in the g,r,z bands.

3 IMPROVING DES PHOTO-Z USING EBOSS SPEC-Z

3.1 Photo-z of the three eBOSS selections

In this section, we examine the photometric redshifts (z_{ph}) of the eBOSS ELG sample that were obtained by matching the positions of the ANNZ2 photometric redshifts catalogue from Sánchez et al. (2014) with positions of eBOSS targets with spectroscopic redshifts. In Fig. 6, we compare the matched photometric redshifts for the three eBOSS selections, with the secure spectroscopic redshifts. We stress that in this work we are considering only these DES galaxies that are cross-matched with the eBOSS emission line galaxy sample.

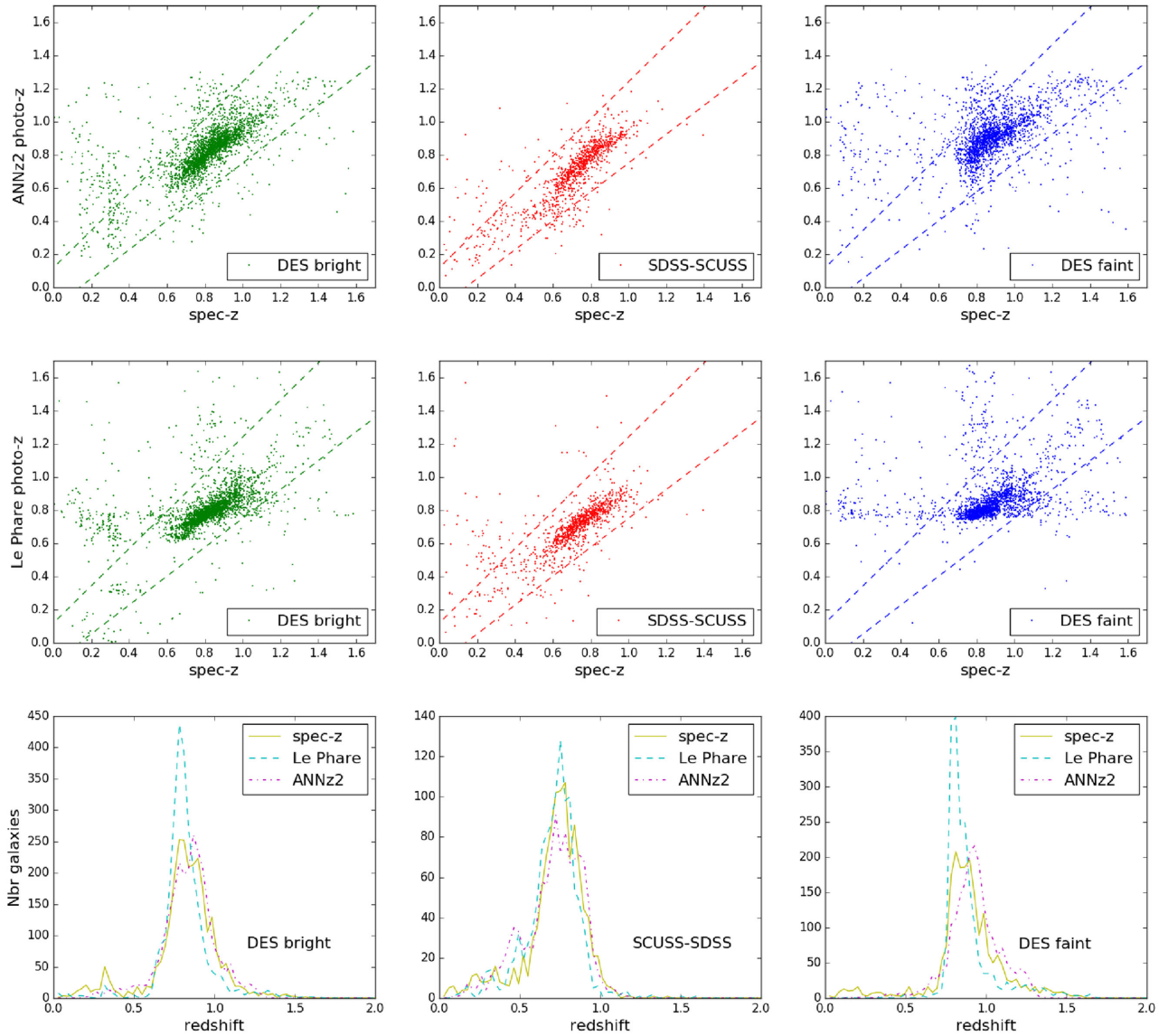

Figure 6. Comparison of photometric to spectroscopic redshifts for the three eBOSS target selections. The top row shows the photometric redshifts using ANNZ2, whilst the bottom row show the photometric redshifts obtained from LE PHARE. Each code was run on the five-band DES SVA1 photometry. The dashed line for the top and bottom panel shows the expected DES accuracy of $|z_{\rm ph} - z_{\rm sp}| = \sigma_{\rm DES}(1 + z_{\rm sp})$ where $\sigma_{\rm DES} = 0.12$.

As such we are considering only a subset of the DES population. An examination of the full DES population is presented in Sánchez et al. (2014). Note that the DES galaxies in the subset that we are considering are typically prone to having photo-z with larger uncertainties.

The SDSS-SCUSS selection has better photometric redshifts than the DES bright and faint selections as indicated in Table 3. SDSS-SCUSS galaxies are targeted using the SDSS photometry, which is shallower than the DES photometry. Fig. 3 shows that SDSS-SCUSS targets are redder in $g - r$ than the targets from the DES selections. SDSS-SCUSS targets are typically redder in $g - r$ colour, compared to DES targets, and as such typically have stronger Balmer and 4000 Å breaks. This allows for an easier redshift measurement, particularly for galaxies at $z < 1$. The SDSS-SCUSS $r - i$ and $r - i/g - r$ colour selections help to exclude galaxies with power-law SEDs, which are more difficult to locate in redshift space. Figs 3 and 6 show that the DES selections, which do not incorporate such colour selections, will lead to a higher rate of outliers than the SDSS-SCUSS selection.

Table 3 shows the mean and median $z_{\rm ph}$, standard deviation, Normalized median absolute deviation (NMAD) and outliers fraction of the $z_{\rm ph} - z_{\rm sp}$ distribution as a function of g-band magnitude for the three selections. NMAD is the normalized median absolute deviation defined as $1.48\ {\rm med}|(z_{\rm ph} - z_{\rm sp})/(1 + z_{\rm sp})|$. NMAD is a measure of the dispersion $z_{\rm ph} - z_{\rm sp}$.

The two rows in Fig. 6 show the photometric redshifts obtained using two different estimators: LE PHARE (bottom row) and ANNZ2 (top row). ANNZ2 and LE PHARE photometric redshifts have similar performances, although LE PHARE has a tendency to aggregate galaxies at $z_{\rm ph}$ 0.8. This is a feature caused by the discretization of the redshift-template parameter space, which is common to most template fitting methods.

Table 3. ANNZ2 DES photometric redshifts results for the three eBOSS selections. The DESz selection corresponds to the DES targets selected at $0.6 < z_{sp} < 1.2$. The purpose of the DESz selection is to show the photo-z quality at high redshift, redshift higher than 0.6.

		DES bright	DES faint	SDSS-SCUSS	DESz bright	DESz faint	SDSS-SCUSSz
$20.5 < g < 22$	$\bar{z_{ph}}$	0.72	0.8	0.63	0.8	0.83	0.71
	Median (z_{ph})	0.74	0.82	0.67	0.79	0.85	0.72
	$\sigma[z_{ph} - z_{sp}]$	0.21	0.3	0.12	0.14	0.2	0.09
	NMAD$[z_{ph} - z_{sp}]$	0.07	0.11	0.04	0.05	0.08	0.03
	Outliers	101	71	10	43	40	5
$22 < g < 23$	$\bar{z_{ph}}$	0.85	0.93	0.7	0.85	0.92	0.75
	Median (z_{ph})	0.85	0.92	0.72	0.85	0.92	0.75
	$\sigma[z_{ph} - z_{sp}]$	0.15	0.22	0.11	0.1	0.13	0.09
	NMAD$[z_{ph} - z_{sp}]$	0.04	0.05	0.04	0.03	0.04	0.03
	Outliers	187	223	37	83	104	21
$20.5 < g < 23$	$\bar{z_{ph}}$	0.83	0.91	0.69	0.84	0.91	0.74
	Median (z_{ph})	0.84	0.92	0.72	0.84	0.91	0.75
	$\sigma[z_{ph} - z_{sp}]$	0.17	0.23	0.11	0.11	0.14	0.09
	NMAD$[z_{ph} - z_{sp}]$	0.04	0.06	0.04	0.03	0.05	0.03
	Outliers	288	294	47	126	144	26

3.2 Reducing the outlier fraction: template fitting versus neural networks

In the context of the DES survey, we investigate possible ways to reduce the redshift outliers fraction. ELGs are the most difficult galaxy population for measuring accurate z_{ph}. ELGs typically constitute a large percentage of outliers. We take advantage of the eBOSS sample to look at possible ways of calibrating and reducing the outliers fraction. One solution, proposed by Newman et al. (2013), involves comparing the photometric redshifts returned by template fitting methods with those from machine learning techniques. Outliers are pruned by searching for large differences between the results returned for each of these methods. We demonstrate this using the DES-eBOSS data in the top panel of Fig. 7, which shows the difference between the spectroscopic redshifts and the photometric redshifts estimated by LE PHARE and the difference between the redshifts from LE PHARE and those from ANNZ2. Accurate photometric redshifts are located inside the black lines. The red lines show a possible template fitting versus machine learning criterion at $|\text{ANNZ2 - LE PHARE}| = 2\sigma_{\text{DES}}$, where $\sigma_{\text{DES}} = 0.12$ is the expected accuracy for the DES survey. Selecting the galaxies inside the red lines is a possible way to prune from outliers. It will however remove some galaxies for which we have a good photometric redshift. With this approach one had to therefore make a compromise between having a sample that is clean and free of outliers, and having a complete sample, which retains more galaxies but at the expense of having a higher outlier rate. The bottom panel of Fig. 7 shows the change in completeness and outlier rate (from the outlier population) as a function of the threshold difference applied in pruning the data set. The solid blue line shows the percentage of outliers pruned from the total outlier population by the selection criteria. Outliers are defined as $|\text{LE PHARE} - z_{sp}| > 2\sigma_{\text{DES}}$. The completeness shows the percentage of galaxies with a reliable photo-z left in the sample. A selection criterion at $2\sigma_{\text{DES}}$ prunes about 30 per cent of outliers and a galaxy sample complete at 92 per cent. Carrasco Kind & Brunner (2014) gives a more detailed investigation of this approach.

3.3 Reducing the outliers fraction using random forest

3.3.1 The TPZ algorithm

We now investigate a new method to reduce the outlier fraction using TPZ (Trees for Photo-Z) (Carrasco Kind & Brunner 2013). TPZ is a machine learning algorithm that uses prediction trees and random forest techniques to find a photometric redshift. TPZ implements two methods: classification or regression trees. We used regression trees that starts with an initial training sample and splits it into branches. The split follows a minimization of the squared errors at a given node. It then splits into two branches unless the minimum number of galaxies in a leaf was reached. We defined a minimum of 20 galaxies per leaf. We did not try to optimize this number. TPZ also bootstraps the training sample to generate several prediction trees and combines their predictions to decide of the best way to split at a node, this is the random forest process. We give TPZ the DES magnitudes g,r,i,z and colours $g - r$, $r - i$, $i - z$ with the eBOSS spectroscopic redshifts. Fig. 8 shows an example of tree from TPZ with the DES-eBOSS data.

3.3.2 Results of TPZ on the eBOSS ELG sample

We randomly selected half of the DES-eBOSS spec-z sample to be the training set, with the remaining half as the testing set. We then examine the percentage of outliers in each branch of the tree generated with TPZ. The top panel of Fig. 9 shows the number of galaxies as a function of the outlier fraction. The colour density corresponds at the number of branches that have the same number of galaxies and outlier fraction. We observe that some branches have a high percentage of outliers.

Same as in Section 3.2, there is a tradeoff between the number of branches one can prune and the completeness of the resulting galaxy sample. The bottom panel of Fig. 9 shows the percentage of galaxies and outliers left in the sample as a function of the value of the percentage chosen for the outliers selection criterion used to trim the branches. For example, if we exclude the branches

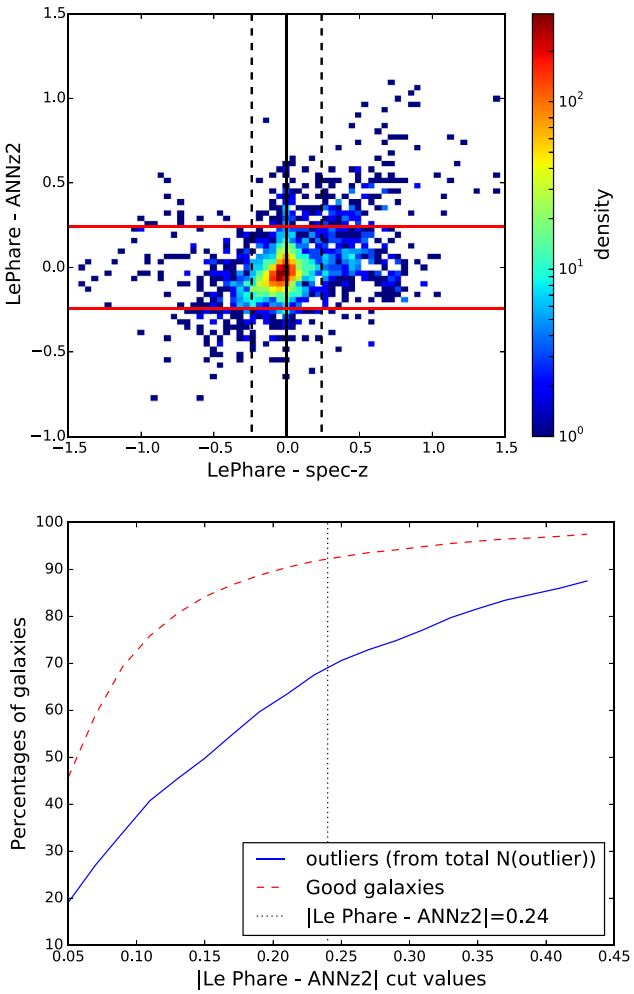

Figure 7. The top panel demonstrates a method to reduce the number of outliers by pruning the data set to exclude those galaxies that have a large difference between photo-z returned by template fitting and machine learning methods. The dashed black lines and red solid lines show $2\sigma_{\rm DES}$: twice the expected accuracy of DES. The bottom panel shows the change in the completeness of the sample (red dashed line) as a function of pruning threshold |LE PHARE - ANNZ2|. The blue solid line shows the outlier fraction from the total outlier sample as a function of pruning threshold |LE PHARE - ANNZ2|.

that have more than 40 per cent of outliers, we have a galaxy sample complete at 85 per cent and decrease the outlier fraction by 50 per cent (depending on which photometric redshift code is used to define the outliers).

We note that the number of outliers in this sample is around 1 per cent as shown in Tables 2 and 3. The black solid line, blue dashed line and green dash–dotted line, we respectively show the results for TPZ, LE PHARE and ANNZ2. We note that this method relies on having a spectroscopic training sample (i.e. the eBOSS observations), and that this sample then defines the branches with reliable photo-z estimation. We stress here that Sections 3.2 and 3.3 show a photo-z point of view. Some data analysis will want a distance estimate $p(z)$ for each galaxy without the need of $N(z)$, for example the analysis of clusters. In this case, being able to identify outliers by comparing photo-z methods such as explained in Section 3.2 is useful. From a clustering point of view, we need to understand the sample of galaxies being removed. Then the method presented in Section 3.3 is more interesting since we remove galaxies by

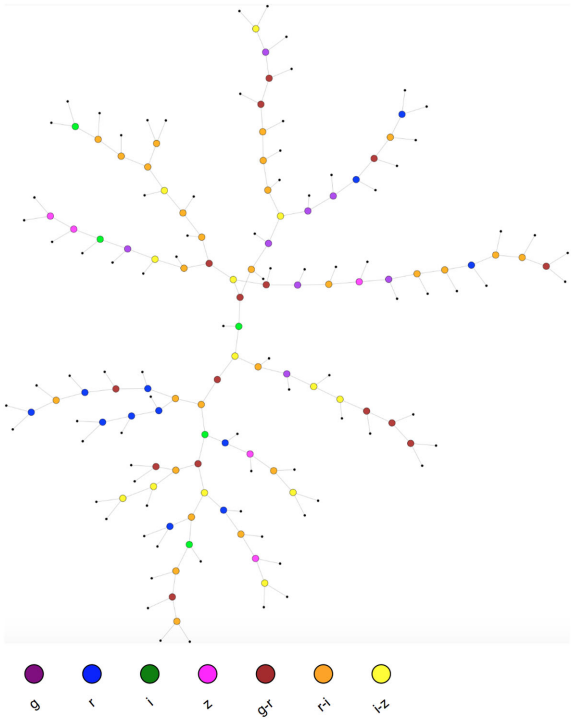

Figure 8. Example of TPZ tree obtained from the DES-eBOSS data. The colours represent the dimension used for the split at the node.

branches, which are designed from the random forest algorithm. A drawback of this method is that spectroscopic surveys have a high incompleteness when compared to photometric surveys. This method would potentially lead to removing large part of the photometric sample. More analysis are needed to better understand the impact of such selections on clustering analysis. We stress again that these sections have been written from a photo-z point of view. We note that the clustering Section 4 do not use those selections.

4 CLUSTERING PROPERTIES

In this section, we measure the monopole of the spatial correlation function, as well as the projected angular correlation function for two of the proposed ELG selections, the DES bright and DES faint selections. The SDSS-SCUSS selection will be presented in a separate work in preparation.

The effective area of the footprint is 9.2 deg^2. We have selected in both samples, only those galaxies with secure and 1 line redshift to be in the redshift range $0.6 < z_{\rm sp} < 1.2$ and that are visible in the DES footprint given by the angular mask, as detailed below.

For the bright sample this represents 71.6 per cent of the observed sample and for the faint sample 68 per cent of the observed sample. The number of ELGs in the final sample, the mean density and mean redshift for the bright and faint sample used in this section are shown in Table 4. The faint sample effectively selects a more distant sample, with mean redshift at $z = 0.9$ (in comparison with the bright sample at $z = 0.855$) although with a worse efficiency.

In addition to the spectroscopic bright and faint sample, we calculate the monopole of the spatial correlation function for a photometrically selected bright and faint sample, using the redshifts given by ANNZ2 and LE PHARE. Comparing these samples with the spectroscopic samples, we investigate how the ELG clustering signal will be seen in DES. In Table 4, we show the number of ELGs, the

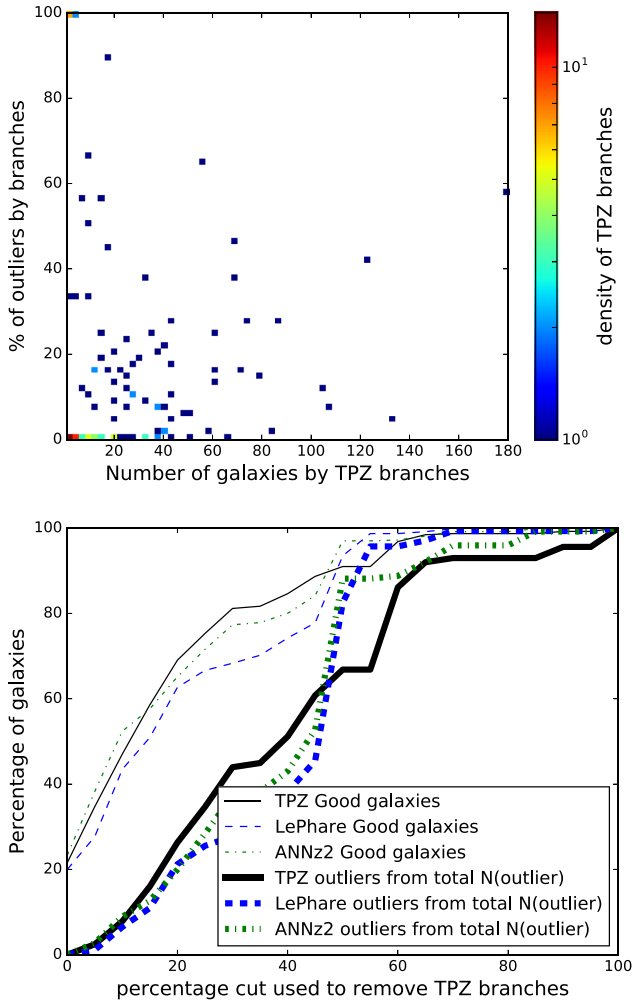

Figure 9. Application of random forest algorithm to DES colours to find outliers. The top panel shows the number of galaxies as a function of the percentage of outliers by branches. We define outliers as the galaxy sample for which $z_{ph} - z_{sp} > 2\sigma_{DES}$. The colour bar shows the density of branches. The bottom panel shows the number of galaxies and outliers remaining (from the total sample of outliers) as a function of the value of the outlier fraction chosen to trim the branches.

Table 4. Mean statistics for the bright and faint sample used in this section. The z_{sp} selection have been obtained selecting ELGs with secure and 1*line* spectroscopic redshift $0.6 < z < 1.2$, while the ANNZ2 and LE PHARE samples have been selected using their respective photometric redshift measurement in the same photometric redshift range. These numbers were obtained after the catalogue was pruned by the angular mask, as detailed below.

	Number (purity)	Mean density	Mean redshift
		Bright	
z_{sp}	2613 (100 per cent)	284.02 gal deg^{-2}	0.855
ANNZ2	2902 (86.66 per cent)	315.43 gal deg^{-2}	0.866
LE PHARE	3038 (84.10 per cent)	330.22 gal deg^{-2}	0.811
		Faint	
z_{sp}	2139 (100 per cent)	232.50 gal/ deg^{-2}	0.901
ANNZ2	2582 (79.43 per cent)	280.65 gal deg^{-2}	0.928
LE PHARE	2662 (77.23 per cent)	289.35 gal deg^{-2}	0.841

mean density and mean redshift for these photometric selections. In these samples, we also look at the purity of ANNZ2 and LE PHARE in selecting galaxies in the redshift range of interest. In this case we define purity as the number of sources selected with a given photometric redshift code, with spectroscopic redshift in the range $0.6 < z_{sp} < 1.2$. For example, for the bright sample, 87 per cent of the sources selected with ANNZ2 in the range $0.6 < z_{ph} < 1.2$ are in $0.6 < z_{sp} < 1.2$. Table 4 shows that the neural network redshift code ANNZ2 has a slightly better performance than LE PHARE since it produces counts and number densities that more closely resemble those from the sample with spectroscopic redshifts. Also, both algorithms worked better for the bright than for the faint sample. It is important to note that in order to calculate the monopole for the photometric samples, we will use their spectroscopic redshifts to obtain distances, and not their photometric redshifts. The redshift distribution for the samples under analysis are shown on the left panel of Fig. 10, together with the redshift distribution for the randoms used in the measurement of the correlation functions. The randoms have been computed considering the different depths of the DES survey, and the process is detailed next.

Throughout this analysis we assume a flat Λ cold dark matter $+ \nu$ (one massive neutrino) cosmological model based on *Planck* 2013 + *WMAP* polarization + ACT/SPT + BAO, with a total matter density relative to critical $\Omega_m = 0.307$, $\sigma_8 = 0.8$ (Planck Collaboration XVI 2014).

4.1 Random fields

The DES observes at different depths, indicating that the measured density of galaxies in the catalogue cannot be translated directly into the mean density of galaxies. In general, we will observe more galaxies in regions where the survey is deeper and less galaxies where the survey is shallower. This information must be encoded into the random catalogue to avoid misinterpretation of the galaxy clustering signal.

We use the MANGLE mask of the DES survey (Fig. 2) in the observed field to create a random catalogue, sampling the footprint with the same depth, angular distribution and ELG selections. We use the g band as the only detection band to which we define the magnitude limit, as imposed by the target selection (see target selection in Section 2.4). The magnitude limit distribution for the analysed area is shown in the first panel of Fig. 2 in units of magnitude for a 2 arcsec aperture at 10σ.

We first select regions inside the mask with limiting 2 arcsec aperture magnitude in g band between $23.4 < \text{mag} < 25.8$. With this cut, we ensure a negligible loss of area. The final effective area continues to be 9.2 deg^2.

We now proceed to generate the random catalogues following the depth and angular footprint of the MANGLE mask.

In order to generate non-uniform random catalogues corresponding to the variations in depth, we apply the following methodology:

(i) Create a uniform random catalogue following the angular footprint of the mask.

(ii) Associate the galaxy and random catalogues to the properties of the mask, polygon where they lay in. Retrieve the information about the area and the depth in band g, given in the mask for each source in both catalogues.

(iii) Study the distribution of galaxies as a function of MANGLE depth. Generate number of galaxies bins in several ranges of g band from 23.4 to 25.8.

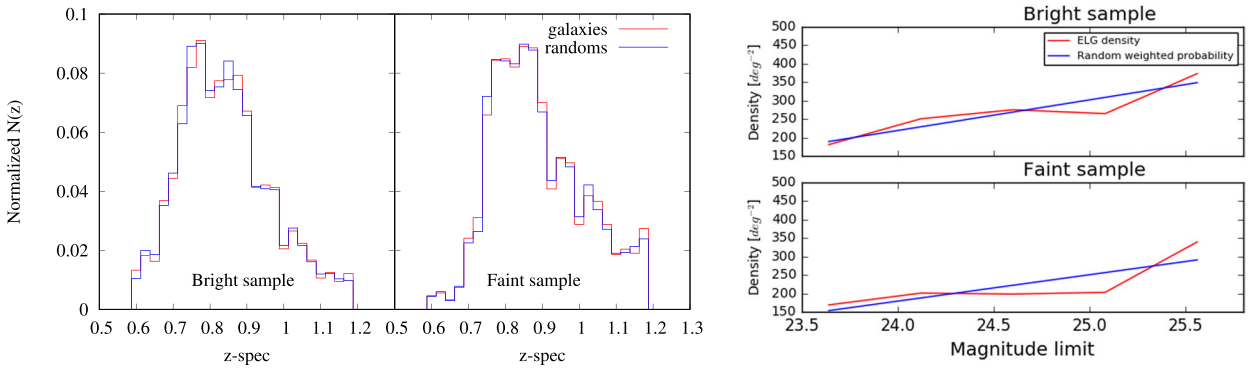

Figure 10. Left figure shows the redshift distribution for the ELG bright and faint samples, superimposed to their corresponding random samples used in the calculation of the correlation functions. The modelling of the randoms is discussed in Section 4.1. Right figure shows the ELG density (blue lines) as a function of magnitude limit in g band for the bright (upper panel) and faint (bottom panel) samples. Red lines show the polynomial fit used to assign weights to the random catalogues, once we normalize it to 1 at its maximum $m = 25.8$. For some intermediate magnitude limits, there is an apparent decrease in density. This is definitely a variance effect, due to the small area observed in a very in-homogeneous footprint and the small number of ELG targets.

(iv) Build the density distribution in each depth bin as the number of galaxies over the area (information given by MANGLE) and generate the density function, i.e. the density as a function of depth.

(v) Create the probability function according to

$$P[i] = \frac{\int_{m^i_{\rm min}}^{m^i_{\rm max}} \rho(m)\,{\rm d}m}{\int_{m^{\rm tot}_{\rm min}}^{m^{\rm tot}_{\rm max}} \rho(m)\,{\rm d}m}, \quad (1)$$

where $m^i_{\rm max}$ and $m^i_{\rm min}$ are the maximum and the minimum values of the depth in the bin i and $m^{\rm tot}_{\rm min}$ and $m^{\rm tot}_{\rm max}$ are the initial and final depth according to the binning used. In our case, $m^{\rm tot}_{\rm max} = 25.8$ and $m^{\rm tot}_{\rm min} = 23.4$.

(vi) Assign a probability to random points according to the magnitude limit.

(vii) Assign a random value in the interval $(0 - 1]$ for each random point and compare with the probability given in the previous step. We accept the random point if random value is smaller than the probability and reject it otherwise.

On the right-hand panel of Fig. 10, we show both the ELG density as a function of magnitude limit in g band, as well as the probability distribution as a function of magnitude limit in g band for the randoms, based on the steps above, for both the bright and faint sample. This measurement is very limited by sample variance. None the less, we approximate the density distribution by a first-order polynomial to assign reject/acceptance probabilities as a function of magnitude limit for the random samples. We find a mean error of 8 per cent for each of the ELG probability densities estimated using the variance cookbook (Moster et al. 2011) with similar survey configurations as COSMOS.

With the probability distribution as a function of depth and position in the footprint, we can now calculate the random sample used throughout the following analysis, after we model the ELG redshift distribution. In both samples, we calculate approximately 2.8×10^6 random points.

We model the line-of-sight redshift distribution of the bright and faint random samples based on the ELG distributions shown on the left-hand panel of Fig. 10. We transform the redshift distribution into a probability distribution function and use this to assign redshifts to the random sample. We do not consider the existing correlation between depth and redshift range. As deeper regions reach higher redshifts, this might be an important effect when we move to future larger data releases. For now, we ignore this effect since we are mostly limited by cosmic variance. The redshift distributions for galaxy data and randoms used in the analysis are shown on the left-hand panel of Fig. 10.

We have verified that a non-uniform random constructed from the MANGLE mask has no correlation with itself, whereas a random that is uniform in magnitude correlates with the data on small scales. This indicates that our random is appropriate for the clustering analysis, whereas a uniform random is not. We have also applied our methodology for generation of randoms to simulations of the DES and found that the correlations measured are consistent with the theoretical results.

Another possible approach would be to perform a more conservative analysis and lower the magnitude limit such that field-to-field variations become negligible (see e.g. Kim et al. 2014). Since this would decrease even further the size of our galaxy sample, we decided to account for the observed magnitude limit variations, as these were readily available from the MANGLE mask.

4.2 Two-point spatial correlation function

We estimate the two-point spatial correlation function (2PTCF) via the Landy and Szalay (LS, Landy & Szalay 1993) estimator under the fiducial cosmology on scales $1 < s < 50$ Mpc h^{-1} using the CUTE code[6] (Alonso 2015) and compute the galaxy bias for the considered samples. Throughout this section, we use the letter s to refer to scales in redshift space for the 2PTCF monopole computation.

The Poisson errors associated with LS estimator underestimate the actual uncertainty in the correlation function. Following Xu et al. (2012), here we consider a theoretical estimation for the covariance of the spatial 2PTCF assuming Gaussianity and a linear independent evolution of Fourier modes of the matter field overdensity,

$${\rm Cov}_\xi(r, r') = \frac{2}{V}\int_0^\infty {\rm d}k\ \frac{k^2}{2\pi^2} j_0(kr) j_0(kr') \left[P(k) + \frac{1}{\bar{n}}\right]^2, \quad (2)$$

where V is the volume of the sample and $\bar{n}$ represents the mean number of galaxies per volume unit, accounting for the shot noise (SN).

To take into account the effect of binning on the estimates of the 2PTCF and its covariance we spherically average them inside

[6] https://github.com/damonge/CUTE

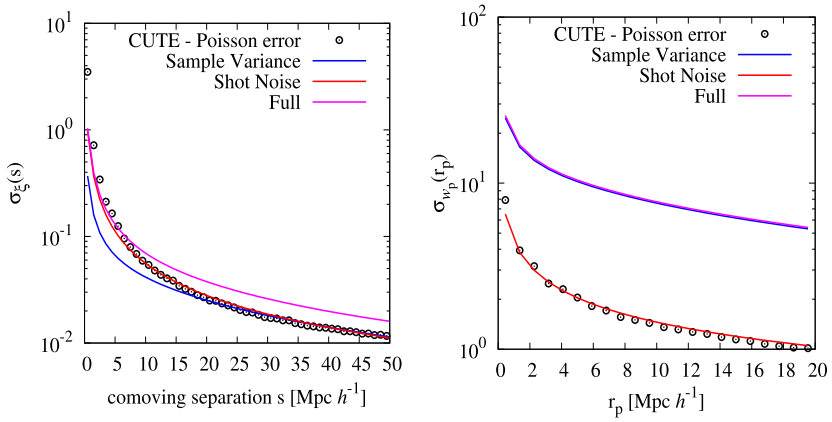

Figure 11. Contributions to the 2PTCF error estimates. Black circles represent the LS estimate for the pure Poisson error. Continuous curves show theoretical estimates of Gaussian and linear variance computed according to equation (2). The pure SN contribution had been isolated (red curve) from the sample variance-dependent part (blue curve) in order to be compared with the LS Poisson error estimate. The agreement of SN and LS estimates is consistent with the interpretation of Poisson error as the number of data–data pairs estimated per bin. The full estimate from equation (2) (magenta curve) is the error estimate used on the analysis presented.

each considered bin following Xu et al. (2012). For the scales and bin-width considered, the effect of binning on the 2PTCF itself is negligible, the same applies to the contribution of the power spectrum to the theoretical covariance, equation (2), but it is not true for its pure SN contribution, i.e. the resulting of only considering the term proportional to $\bar{n}^{-2}$, which is intrinsically diagonal and divergent. However, this property comes from the fact that equation (2) applies only in a continuous limit, i.e. for infinitesimal bin widths. After taking the spherical average of such contribution to the covariance we have,

$$\mathrm{Cov}_\xi^{\mathrm{SN}}(r_n, r_m) = \frac{2}{V}\frac{1}{4\pi}\left[\frac{3}{r_{n+1}^3 - r_n^3}\right]\frac{\delta_{mn}}{\bar{n}^2}. \quad (3)$$

A comparison of the contribution to the square root of the variance of the 2PTCF is shown on the left-hand panel of Fig. 11, where the SN contribution has been isolated in order to be compared with the Poisson error resulting from LS estimation according to CUTE code (circle points). An agreement is observed between this two estimates, this is consistent with the interpretation of Poisson variance coming from the number of data-data pairs estimated per bin.[7] Note that the curves shown under Sample Variance label in Fig. 11 represent all contributions to the 2PTCF variance except the pure SN one, equation (3).

The left-hand panel of Fig. 11 shows that the effect of sample variance could have an impact in the error budget for our analysis even by assuming the simple case of Gaussian and linear covariance. Consequently, throughout the rest of our analysis we consider its effect via the theoretical treatment described above. It is indeed important to mention that a more precise analysis of the clustering signal will require the creation of mock catalogues both for a more precise calculation of the covariance, and in a bigger volume to have a significant clustering value.

On the error estimates, in addition to the sample variance, we also account for the effects of the finite volume of the sample by estimating an integral constraint factor (IC). For this purpose, we measured random–random pairs from the random catalogues, RR(s), up to the maximum separation allowed by the sample volume and, following Roche & Eales (1999), we estimate IC as

$$\mathrm{IC} = \frac{\sum_i \xi(s_i)\mathrm{RR}(s_i)}{\sum_i \mathrm{RR}(s_i)}, \quad (4)$$

modelling the clustering signal on the spatial 2PTCF, $\xi(s)$, as a single power law of the form

$$\xi(s) = \left(\frac{s}{s_0}\right)^{-\gamma}. \quad (5)$$

We consider two approaches to fit the power law, equation 5 to the data: (i) by subtracting the IC from the model and (ii) by allowing it to vary with the model parameters. We checked that these two approaches are consistent with each other with an iterative procedure for the first one, in which we first fit a model to the original data, then use this model to estimate a correction via equation 4, and apply this correction to the data. We repeat the process to the new data until convergence is achieved. In our case, convergence was always reached in less than 20 iterations. Note however that by using the second approach, fitting the model and IC correction simultaneously, we avoid the need for correcting the data.

This single power-law model represents reasonable approximation for comoving scales in the range $1 < s < 20\,h^{-1}$ Mpc. We considered different maximum scales between 10 and $50\,h^{-1}$ Mpc to perform the fit and found that the results are insensitive to this scale. None the less $20\,h^{-1}$ Mpc was chosen because (i) at the redshifts of interest, the linear regime extends up to this scale and (ii) for scales below $20\,h^{-1}$ Mpc, the amplitude of measured $\xi(s)$ is always one order of magnitude larger than our estimates of the IC.

We apply the model above to the spectroscopically selected ELG bright and faint samples, to the photometrically selected catalogues using ANNZ2 and LE PHARE photo-z codes, and to some of the pruned catalogues presented in Section 3.2. Our results are shown in Table 5. The z_{sp} samples are selected with spectroscopic redshifts between 0.6 and 1.2. ANNZ2 and LE PHARE are samples selected in the same redshift range but using their photo-z value. For the bottom lines of table, we use the photo-z values and a cut $|\mathrm{LE\ PHARE} - \mathrm{ANNZ2}| < 0.24$, which is presented in Section 3.2. However, we use their true redshift, and not the photo-z, to compute

[7] For the smallest scales, Fig. 11 shows that the estimate of SN contribution via equation (3) underestimates the Poisson contribution from LS. This is indeed expected given that here we are considering pure linear SN contribution (see e.g. section 3.2 of Xu et al. 2012).

Table 5. 3D clustering properties of faint and bright samples selected using the different redshift estimates. Single power-law model for the 3D 2PTCF (equation 5) parameters were constrained in the range $1 < s < 20\,h^{-1}$ Mpc. The integral constraint correction (IC) was modelled according to equation (4) and is for all cases presented one order of magnitude lower than the 2PTCF for the considered scales.

Sample	Redshift selection	s_0 (h^{-1} Mpc)	γ	IC	χ^2/d.o.f.
Faint	z_{sp}	$5.13^{+0.17}_{-0.17}$	$1.301^{+0.050}_{-0.054}$	0.014	0.594
	ANNz2	$5.42^{+0.14}_{-0.17}$	$1.260^{+0.043}_{-0.044}$	0.017	1.03
	LE PHARE	$5.35^{+0.16}_{-0.15}$	$1.244^{+0.044}_{-0.046}$	0.018	0.896
	ANNz2 $\lvert$LE PHARE$-$ANNz2$\rvert < 0.24$	$5.64^{+0.14}_{-0.16}$	$1.272^{+0.041}_{-0.043}$	0.017	1.36
	LE PHARE $\lvert$LE PHARE$-$ANNz2$\rvert < 0.24$	$5.54^{+0.15}_{-0.15}$	$1.252^{+0.043}_{-0.044}$	0.018	1.12
Bright	z_{sp}	$5.23^{+0.16}_{-0.15}$	$1.213^{+0.044}_{-0.044}$	0.019	0.741
	ANNz2	$5.74^{+0.13}_{-0.14}$	$1.212^{+0.036}_{-0.039}$	0.021	1.02
	LE PHARE	$5.66^{+0.13}_{-0.15}$	$1.211^{+0.034}_{-0.037}$	0.021	1.05
	ANNz2 $\lvert$LE PHARE$-$ANNz2$\rvert < 0.24$	$5.80^{+0.14}_{-0.14}$	$1.208^{+0.038}_{-0.038}$	0.021	1.18
	LE PHARE $\lvert$LE PHARE$-$ANNz2$\rvert < 0.24$	$5.82^{+0.15}_{-0.15}$	$1.174^{+0.035}_{-0.035}$	0.02	1.23

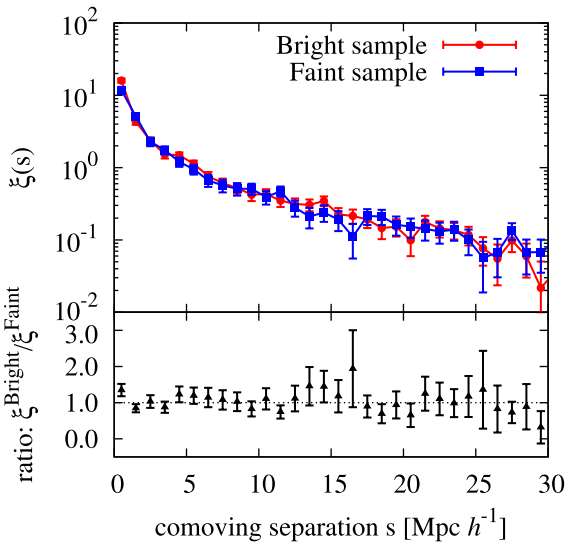

Figure 12. Comparison of the 3D 2PTCF $\xi(s)$ for the faint and bright samples. The top panel shows the measured correlations. The bottom panel displays the ratio between bright and faint samples.

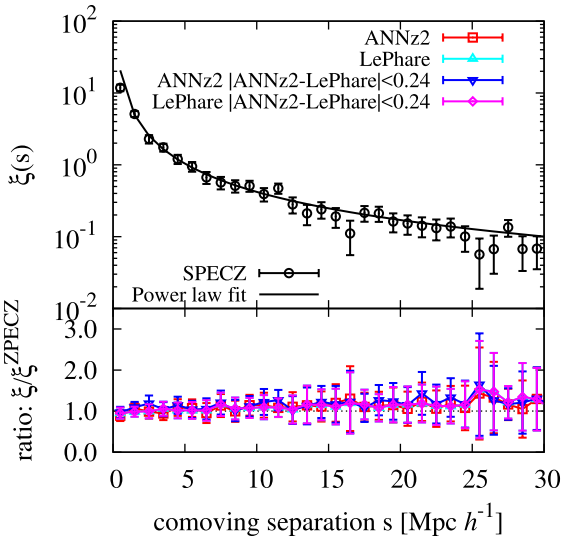

Figure 13. Comparison of $\xi(s)$ for different redshift selections for the faint sample only. The top panel shows the monopole for the clean z_{sp} sample between $0.6 < z < 1.2$. The bottom panel shows the ratio between different redshift selections and the clean sample. An apparent increase on the clustering at large scales is seen for the photometric redshifts selections.

distances and in $\xi(s)$. This way, we can study selection effects from the photo-z results.

A comparison of the clustering amplitudes for the bright and faint samples is shown in Fig. 12. The error bars were computed by propagating the uncertainties on the 2-point correlations. We see a statistical preference for the clustering amplitude of the bright sample to be higher than the one of the faint sample. This is consistent with the fitted power-law parameters in Table 5. The bright sample has higher values for clustering length s_0 than the faint sample, while the slope γ seems more similar between samples.

Fig. 13 compares the amplitudes of $\xi(s)$ when z_{ph} are considered with respect to the spectroscopic selection.

As we are limited by the sample size and large error bars, no significant comparison is made between the clustering properties of the spectroscopic and photometric samples. There is a slight increase on the clustering correlation when photo-zs are used, which may be a result of competing scatter effects due to photo-z errors.

For the present catalogues, the sample variance and the IC contributions are significant sources of errors, but as the sample grows in size, it should be possible to investigate in detail the effects of photo-z selection in the angular correlation function. We plan to assess the impact of propagating photo-z errors into angular correlations for future larger ELG catalogues from joint eBOSS/DES observations.

After investigating the monopole for these samples, beyond the spectroscopically selected ones, we focus again solely in the spectroscopic bright and faint ELG science samples, where we will measure the mean galaxy bias in the projected angular correlation function.

4.3 Galaxy bias

We measure a mean galaxy bias for the bright and faint samples separately. The samples span a large redshift range $0.6 < z < 1.2$. The meaning of the bias obtained must be taken with caution, as it is an average over a long cosmic time. We roughly assess the

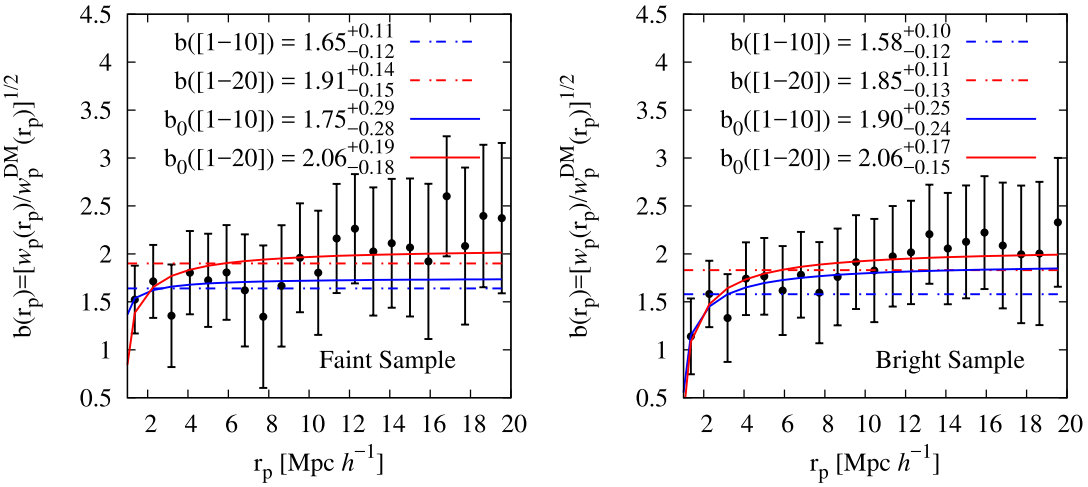

Figure 14. The galaxy bias calculated using a constant and a scale-dependent relation for the faint (left) and bright (right) sample, measured from projected correlation function. In dashed lines, we show the bias value calculated as the average between h^{-1} and $10\,h^{-1}$ Mpc (blue) and between h^{-1} and $20\,h^{-1}$ Mpc (red). The straight lines are a scale-dependent bias fitting to $b(r_p) = b_0 + b_1/r_p$, such that b_0 intends to represent a large-scale bias. The results depend on the range of scales used in the average and in the limiting value of the fit. For comparison to previous studies, we select the averaged bias between h^{-1} and $10\,h^{-1}$ Mpc (dashed blue) as our bias proxy, but we note that different definitions gives different results.

galaxy bias evolution by comparing the results for the bright and faint samples, which are at slightly different mean redshifts. As a result, we estimate the absolute magnitude limit that DES reaches when selecting ELGs.

In order to account for redshift space distortions, we follow the results from the VIPERS clustering analysis (Marulli et al. 2013) and estimate the galaxy bias for our samples using the projected real space correlation function $w_p(r_p)$.

We first estimate the anisotropic 2PTCF, $\xi(r_p, \pi)$, in the spatial ranges $\pi \in [1, 40]$ h^{-1} Mpc and $r_p \in [1, 50]$ h^{-1} Mpc using the LS (Landy & Szalay 1993) estimator under the fiducial cosmology using the CUTE code and integrate along the line of sight, π, to estimate $w_p(r_p)$ for all samples,

$$w_p(r_p) = 2\int_0^\infty d\pi' \xi(r_p, \pi'), \tag{6}$$

where $\xi(r_p, \pi') = \xi(s = \sqrt{\pi'^2 + r_p^2})$ and in practice the line-of-sight integration is taken up to $\pi_{max} = 30\,h^{-1}$ Mpc as in (Marulli et al. 2013).

Then, the galaxy bias is defined as

$$b(r_p) = \sqrt{\frac{w_p(r_p)}{w_p^m(r_p)}}, \tag{7}$$

where $w_p(r_p)$ is given by equation (6) and is obtained from the galaxy sample, while $w_p^m(r_p)$ is the projected matter correlation function. We compute $w_p^m(r_p)$ from the theoretical power spectrum obtained using CAMB (Lewis & Bridle 2002), with the HALOFIT routine (Smith et al. 2003) for non-linear corrections.

Throughout the analysis we assume a passive bias model. This is sufficient considering the small statistics. We note that ELGs are not passively evolved. A more robust bias analysis will be necessary when the sample increase.

As for the case of the 3D 2PTCF, the sample variance on the error in the 2PTCF is considered using the linear theoretical prediction,

$$\mathrm{Cov}_{w_p}(r_p, r_p') = 4\int d\pi \int d\pi' \times \mathrm{Cov}_\xi\left(\sqrt{\pi^2 + r_p^2}, \sqrt{\pi'^2 + r_p'^2}\right), \tag{8}$$

where Cov_ξ is given by equation (2). A comparison of the contribution to the square root of the variance of the projected 2PTCF is shown in the right-hand panel of Fig 11, where, as in the previous section, the pure SN contribution has been isolated in order to be compared with the pure Poisson error resulting from LS estimation according to CUTE code (circle points). As in the 3D 2PTCF, we confirm an agreement between this two estimates. As for the 3D 2PTCF, throughout the rest of our analysis we consider its effect via the theoretical treatment described above.

For comparison with VIPERS (Marulli et al. 2013), the bias is first estimated as the average of $b(r_p)$ in the range of [1–10] h^{-1} Mpc, where the bias is fairly constant, as claimed in VIPERS and shown in Fig. 14. In order to account for a small-scale dependency on the smallest scales, we also fit a relation $b(r_p) = b_0 + b_1/r_p$, such that b_0 is taken as an estimate of the linear large-scale bias.

For both methods used, averaged and scale-dependent bias, Table 6 shows that the results depend on the scales used. The smallest scales bring in non-linearities whereas the largest scales are subject to sample variance, lower signal to noise and the largest possible effects from the IC. We note that we find the constant IC (0.01–0.02) to be an order of magnitude lower than the correlation (0.1–0.2) around 20 h^{-1} Mpc. This 10 per cent effect on the correlation could in principle affect the bias estimation. This effect is smaller around 10 h^{-1} Mpc, where the correlation is a factor of 2–3 larger.

The values for the bias change significantly between the averaged and scale-dependent bias. This indicates a measurable effect of the non-linearity on the smallest scales.

Table 6. Clustering properties and bias for the faint and bright samples selected with spectroscopic redshifts. The clustering length and slope were obtained by fitting a power law for $w(r_p)$ for $0.5 < r_p < 20\,h^{-1}$Mpc. The averaged bias value was obtained by averaging the scale-dependent bias $b(r_p) = [w(r_p)/w_m(r_p)]^{1/2}$, while b_0 comes from a fit to the scale-dependent bias $b(r_p) = b_0 + b_1/r$. Both the average and the fit bias are obtained over scales $1 < r_p < 10\,h^{-1}$Mpc as well as $1 < r_p < 20\,h^{-1}$Mpc.

Sample	s_0 (Mpc h^{-1})	γ	Mean z	Bias averaged up to [10–20] Mpc h^{-1}	χ^2/d.o.f.	b_0 fitted up to [10–20] Mpc h^{-1}
Bright	$4.04^{+0.64}_{-0.95}$	$1.467^{+0.113}_{-0.124}$	0.855	$1.58^{+0.10}_{-0.12}$–$1.85^{+0.11}_{-0.13}$	0.092	$1.90^{+0.25}_{-0.24}$–$2.06^{+0.17}_{-0.15}$
Faint	$4.26^{+0.68}_{-1.02}$	$1.499^{+0.110}_{-0.149}$	0.901	$1.65^{+0.11}_{-0.12}$–$1.91^{+0.14}_{-0.15}$	0.11	$1.75^{+0.29}_{-0.28}$–$2.06^{+0.19}_{-0.18}$

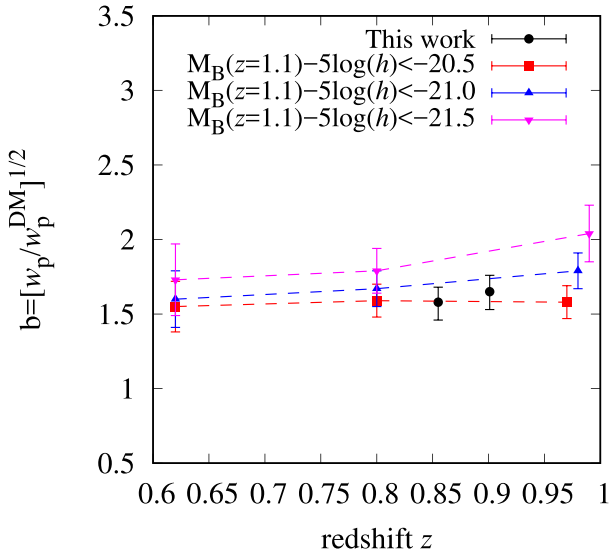

Figure 15. In black, the galaxy bias for our target selection samples in the range $0.6 < z < 1.2$ for the faint and bright. The reference values comes from table 1 of Marulli et al. (2013) from the VIPERS survey. In both cases, biases have been measured as the average in [1–10] h^{-1} Mpc. Our bias agrees within one sigma with a galaxy population brighter than $M_B - 5\log(h) < -20.5$.

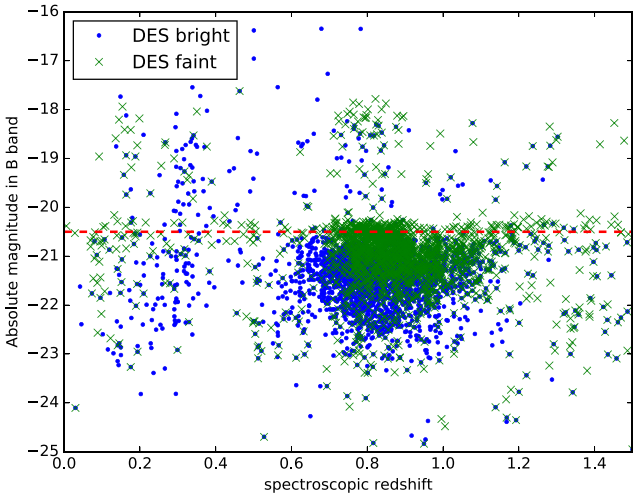

Figure 16. Absolute magnitude in the B band for the ELG spectroscopic sample as a function of spectroscopic redshift. Magnitudes were calculated using LE PHARE with the same configuration as in the photo-z calculation, but using the galaxy spectroscopic redshifts. The population is consistent with a selection $M_B - \log(h) < -20.5$ in the redshift interval $0.6 < z < 1.2$, in agreement with the bias measurement from Fig. 15. This corresponds to 84 and 72 per cent in respectively the bright and faint sample.

The errors have been obtained propagating the uncertainties in r_0 and γ shown in the table, after fitting to (Marulli et al. 2013)

$$w(r_p) = r_p \left(\frac{r_0}{r_p}\right)^{\gamma} \frac{\Gamma(\frac{1}{2})\Gamma(\frac{\gamma-1}{2})}{\Gamma(\frac{\gamma}{2})}. \quad (9)$$

In Fig. 15, we compare our measurements to those published for VIPERS (Marulli et al. 2013). For this comparison, we use our averaged bias as reference to reflect the VIPERS procedure.

Our bias agrees with that from VIPERS for a population brighter than $M_B - \log(h) < -20.5$. To confirm this result, we calculated the absolute magnitude for the faint and bright samples together (there is a strong overlap between both samples) to directly measure the limiting absolute magnitude of our sample. We calculate the absolute magnitude for the B band using the template fitting code LE PHARE, fixing the redshift to its spectroscopic value. We show the B-band absolute magnitude density distribution in Fig. 16 as a function of redshift for the bright and faint sample. The result agrees well with what it is expected from the galaxy bias of the sample. The luminosity dependent clustering will be analysed in more detail in future studies.

5 CONCLUSION

We used 9.2 deg^2 of eBOSS observations to study the properties of different possible ELG target selections. The bright DES *grz* bands selection achieves 73 per cent success rate and 71 per cent in the desired redshift window $0.6 < z < 1.2$. The faint DES *grz* bands selection have slightly lower performances with 66 per cent success rate and 68 per cent in the redshift window. Both selections have a stellar contamination lower than 2 per cent. We find a mean redshift of 0.80 and 0.87 for respectively the bright and faint selection. To prepare for the eBOSS survey, we looked at the possible systematic effects on the power spectrum measurement: stellar photometry contamination, airmass, galactic dust and survey depth across the DES year one data. We find a galaxy density variation lower than 15 per cent for each of these systematic effects, which is the highest fluctuation allowed to avoid damaging measurements. With a target density of 857 gal deg^{-2}, our analysis suggests the DES bright selection will give the most accurate power spectrum measurement with an eBOSS-like survey type.

The outliers fraction is one of the main sources of systematics in cosmic shear and large-scale structure analyses (Bernstein & Huterer 2010). With the 4600 eBOSS spectroscopic redshifts, we investigate possible techniques to identify the photometric redshift outliers. Using the random forest code TPZ, we find that by removing the colour branches with a percentage of outliers higher than 10 per cent, we are left with 10 per cent outliers and a galaxy sample of 71 per cent completeness. Abramo et al. (2012) and Newman et al. (2013) suggest another possible technique to decrease the outliers fraction using a comparison between template fitting and machine learning. Using this technique, we decrease the

outlier fraction by 30 per cent and reduce the galaxy sample by 15 per cent. We investigated the clustering properties of our samples, estimating the 3D two-point correlation function monopole $\xi(s)$ and the projected real space correlation function $w(r_p)$. We computed the large-scale galaxy bias, and found it to be consistent with previous ELG measurements (Marulli et al. 2013; Mostek et al. 2013; Favole et al. 2016). The galaxy bias between the DES bright and faint sample are within 1σ of each other. We find a slightly higher bias for the faint sample compared to the bright that is expected due to redshift evolution. We also looked at the binning effect in clustering analysis when having to define a redshift window with photometric redshifts. Considering that DES will have a good photometric redshifts calibration, we used spectroscopic redshifts to compute correlation functions and use the photo-z to define the 0.6–1.2 redshift window. We do not find significant differences when using spectroscopic and photometric redshifts. We finally compare the mean value of the galaxy bias to the deep spectroscopic survey VIPERS and find that the ELG sample agrees with that of a population brighter than $M_B - \log(h) < -20.5$.

ACKNOWLEDGEMENTS

The authors thank Molly Swanson for her great work and help on MANGLE. HC is supported by Conselho Nacional de Desenvolvimento Científico e Tecnológico (CNPq). AC thanks Fernando de Simoni for useful discussions. AC acknowledges financial support provided by the Programa de Apoio ao Pós-Doutorado (PAPDRJ)/Coordenação de Aperfeiçoamento de Pessoal de Nível Superior (CAPES)/Fundação de Amparo à Pesquisa do Estado do Rio de Janeiro (FAPER) Fellowship. ML is partially supported by Fundação de Amparo à Pesquisa do Estado de São Paulo (FAPESP) and CNPq. FBA acknowledges the support of the Royal society via a RS University Research Fellowship. FS acknowledges financial support provided by CAPES under contract No. 3171-13-2. JC and FP acknowledge support from the Spanish Ministerio de Ciencia e Innovación (MICINN) grant MultiDark CSD2009-00064, Ministerio de Economía, Industria y Competitividad (MINECO) Severo Ochoa Programme grant SEV-2012-0249 and grant AYA2014-60641-C2-1-P. FP wish to thank the Lawrence Berkeley National Laboratory for the hospitality and the Spanish MEC Salvador de Madariaga program, Ref. PRX14/00444.

This paper has gone through internal review by the DES collaboration. We are grateful for the extraordinary contributions of our CTIO colleagues and the DECam Construction, Commissioning and Science Verification teams in achieving the excellent instrument and telescope conditions that have made this work possible. The success of this project also relies critically on the expertise and dedication of the DES Data Management group. Funding for the DES Projects has been provided by the U.S. Department of Energy, the U.S. National Science Foundation, the Ministry of Science and Education of Spain, the Science and Technology Facilities Council of the United Kingdom, the Higher Education Funding Council for England, the National Center for Supercomputing Applications at the University of Illinois at Urbana-Champaign, the Kavli Institute of Cosmological Physics at the University of Chicago, the Center for Cosmology and Astro-Particle Physics at the Ohio State University, the Mitchell Institute for Fundamental Physics and Astronomy at Texas A&M University, Financiadora de Estudos e Projetos, Fundaca o Carlos Chagas Filho de Amparo à Pesquisa do Estado do Rio de Janeiro, Conselho Nacional de Desenvolvimento Científico e Tecnologico and the Minisério da Ciencia e Tecnologia, the Deutsche Forschungsgemeinschaft and the Collaborating Institutions in the Dark Energy Survey.

The DES data management system is supported by the National Science Foundation under Grant Number AST1138766. The DES participants from Spanish institutions are partially supported by MINECO under grants AYA201239559, ESP2013-48274, FPA2013-47986, and Centro de Excelencia Severo Ochoa SEV-2012-0234, some of which include ERDF funds from the European Union.

The Collaborating Institutions are Argonne National Laboratory, the University of California at Santa Cruz, the University of Cambridge, Centro de Investigaciones Energeticas, Medioambientales y Tecnologicas-Madrid, the University of Chicago, University College London, the DES-Brazil Consortium, the Eidgenssische Technische Hochschule (ETH) Zurich, Fermi National Accelerator Laboratory, the University of Edinburgh, the University of Illinois at Urbana-Champaign, the Institut de Ciències de lEspai (IEEC/CSIC), the Institut de Física dAltes Energies, Lawrence Berkeley National Laboratory, the Ludwig-Maximilians Universitt and the associated Excellence Cluster Universe, the University of Michigan, the National Optical Astronomy Observatory, the University of Nottingham, The Ohio State University, the University of Pennsylvania, the University of Portsmouth, SLAC National Accelerator Laboratory, Stanford University, the University of Sussex and Texas A&M University.

Funding for the Sloan Digital Sky Survey IV has been provided by the Alfred P. Sloan Foundation, the U.S. Department of Energy Office of Science and the Participating Institutions. SDSS-IV acknowledges support and resources from the Center for High-Performance Computing at the University of Utah. The SDSS web site is www.sdss.org.

SDSS-IV is managed by the Astrophysical Research Consortium for the Participating Institutions of the SDSS Collaboration including the Brazilian Participation Group, the Carnegie Institution for Science, Carnegie Mellon University, the Chilean Participation Group, the French Participation Group, Harvard-Smithsonian Center for Astrophysics, Instituto de Astrofísica de Canarias, The Johns Hopkins University, Kavli Institute for the Physics and Mathematics of the Universe (IPMU)/University of Tokyo, Lawrence Berkeley National Laboratory, Leibniz Institut für Astrophysik Potsdam (AIP), Max-Planck-Institut für Astronomie (MPIA Heidelberg), Max-Planck-Institut für Astrophysik (MPA Garching), Max-Planck-Institut für Extraterrestrische Physik (MPE), National Astronomical Observatory of China, New Mexico State University, New York University, University of Notre Dame, Observatário Nacional/MCTI, The Ohio State University, Pennsylvania State University, Shanghai Astronomical Observatory, United Kingdom Participation Group, Universidad Nacional Autónoma de México, University of Arizona, University of Colorado Boulder, University of Oxford, University of Portsmouth, University of Utah, University of Virginia, University of Washington, University of Wisconsin, Vanderbilt University and Yale University.

REFERENCES

Abazajian K. et al., 2004, AJ, 128, 502
Abazajian K. N. et al., 2009, ApJS, 182, 543
Abdalla F. B., Mateus A., Santos W. A., Sodrè L., Jr, Ferreras I., Lahav O., 2008, MNRAS, 387, 945
Abramo L. R. et al., 2012, MNRAS, 423, 3251
Adelberger K. L., Steidel C. C., Shapley A. E., Hunt M. P., Erb D. K., Reddy N. A., Pettini M., 2004, ApJ, 607, 226

Ahn C. P. et al., 2014, ApJS, 211, 17
Alonso D., 2015, Astrophysics Source Code Library, record ascl:1505.016
Banerji M. et al., 2015, MNRAS, 446, 2523
Bernstein G., Huterer D., 2010, MNRAS, 401, 1399
Bertin E., Arnouts S., 1996, A&AS, 117, 393
Bonnett C. et al., 2016, Phys. Rev. D, 94, 042005
Calzetti D., Armus L., Bohlin R. C., Kinney A. L., Koornneef J., Storchi-Bergmann T., 2000, ApJ, 533, 682
Carrasco Kind M., Brunner R. J., 2013, MNRAS, 432, 1483
Carrasco Kind M., Brunner R. J., 2014, MNRAS, 442, 3380
Comparat J. et al., 2013, MNRAS, 428, 1498
Comparat J. et al., 2016, A&A, 592, A121
Coupon J., Ilbert O., Kilbinger M., McCracken H. J., Mellier Y., Arnouts S., Bertin E., Hudelot P., 2009, A&A, 500, 981
Crocce M. et al., 2016, MNRAS, 455, 4301
Dark Energy Survey Collaboration, 2016, MNRAS, 460, 1270
Dawson K. S. et al., 2016, AJ, 151, 44
Delubac T. et al., 2017, MNRAS, 465, 1831
Favole G. et al., 2016, MNRAS, 461, 3421
Flaugher B. et al., 2015, AJ, 150, 150
Font-Ribera A. et al., 2014, J. Cosmol. Astropart. Phys., 5, 27
Garilli B. et al., 2014, A&A, 562, A23
Ilbert O. et al., 2006, A&A, 457, 841
Ilbert O. et al., 2009, ApJ, 690, 1236
Ivezic Z., Tyson J. A., Allsman R., Andrew J., Angel R., for the LSST Collaboration, 2008, preprint (arXiv:e-prints)
Jia Y. et al., 2014, MNRAS, 441, 503
Jouvel S. et al., 2011, A&A, 532, A25
Jouvel S., Abdalla F. B., Kirk D., Lahav O., Lin H., Annis J., Kron R., Frieman J. A., 2014a, MNRAS, 438, 2218
Jouvel S., Host O., Lahav O., Seitz S., Molino A., Coe D., Postman M., Moustakas L., 2014b, A&A, 562, A86
Kim J.-W. et al., 2014, MNRAS, 438, 825
Landy S. D., Szalay A. S., 1993, ApJ, 412, 64
Laureijs R. et al., 2011, preprint (arXiv:e-prints)
Le Fèvre O. et al., 2005, A&A, 439, 845
Leistedt B., Peiris H. V., 2014, MNRAS, 444, 2
Lewis A., Bridle S., 2002, Phys. Rev., D66, 103511
Lilly S. J. et al., 2007, ApJS, 172, 70
Lima M., Cunha C. E., Oyaizu H., Frieman J., Lin H., Sheldon E. S., 2008, MNRAS, 390, 118
Marulli F. et al., 2013, A&A, 557, A17
Melchior P. et al., 2016, A&C, 16, 99
Mostek N., Coil A. L., Cooper M., Davis M., Newman J. A., Weiner B. J., 2013, ApJ, 767, 89
Moster B. P., Somerville R. S., Newman J. A., Rix H.-W., 2011, ApJ, 731, 113
Newman J. A. et al., 2015, Astropart. Phys., 63, 81
Newman J. A. et al., 2013, ApJS, 208, 5
Parkinson D. et al., 2012 Phys. Rev. D, 86, 103518
Percival W. J. et al., 2010 MNRAS, 401, 2148
Planck Collaboration XVI, 2014, A&A, 571, A16
Raichoor A. et al., 2016, A&A, 585, 50
Roche N., Eales S., 1999, MNRAS, 307, 703
Ross A. J. et al., 2012, MNRAS, 424, 564
Rozo E. et al., 2016, MNRAS, 461, 1431
Sadeh I., Abdalla F. B., Lahav O., 2016, Astron. Soc. Pac., 128, 104502
Sánchez C. et al., 2014, MNRAS, 445, 1482
Schlegel D. et al., 2011, preprint (arXiv:e-prints)
Smee S. A. et al., 2013, AJ, 146, 32
Smith R. et al., 2003, MNRAS, 341, 1311
Swanson M., Tegmark M., Hamilton A., Hill C., 2012, Astrophysics Source Code Library
The Dark Energy Survey Collaboration 2005, preprint (arXiv:e-prints)
Xu X., Padmanabhan N., Eisenstein D. J., Mehta K. T., Cuesta A. J., 2012, MNRAS, 427, 2146

APPENDIX A: SExtractor PARAMETERS

The SExtractor parameters used in this article are

(i) *SPREAD_MODEL* (*SPREADERR_MODEL*) is a morphology based star–galaxy classifier based on comparing the pixel map of the object in the co-add with the PSF model and a exponential+PSF convolved model.

(ii) *MAG_DETMODEL* and *MAG_MODEL* are magnitudes measured from a fitted shape to the object in the detection image.

(iii) *MAG_APER* is a magnitude measured in a circular aperture of specified diameter, here we use an aperture of 2 arcsec.

APPENDIX B: COMPUTING LIMITING MAGNITUDE WITH MANGLE

For the weighted average method, the co-added flux is calculated as a weighted average summed over all the exposures:

$$F_{\rm tot} = \frac{\sum_i w_i p_i F_i}{\sum_i w_i}, \tag{B1}$$

where F_i is the flux in a single exposure and p_i a rescaling factor so that fluxes have the same photometric calibration, the calibrated flux is $p_i F_i$. The weights are given by

$$w_i = \frac{1}{p_i^2 \sigma^2_{{\rm bg},i}}, \tag{B2}$$

where $\sigma_{{\rm bg},i}$ is the variance present with no signal flux, including the sky background, read noise and calibration uncertainties.

Using Gaussian error propagation, the variance of $F_{\rm tot}$ is given by

$$\sigma^2_{\rm tot} = \left[\sum_i \frac{1}{p_i^2 \sigma^2_{{\rm bg},i}} \right]^{-1}. \tag{B3}$$

To go from the co-added weight map to a magnitude limit, we define the magnitude limit by the flux in a given aperture that exceeds the background noise by a factor of 10, i.e. the 10σ magnitude limit. Once $\sigma_{\rm tot}$ is calculated in each region, we use

$$m_{\rm limit} = m_{\rm ZPcal} - 2.5 \log \left(10 \sqrt{\pi \frac{(D/2)^2}{0.27^2}} \sigma_{\rm tot} \right), \tag{B4}$$

where $m_{\rm ZPcal}$ is the zero-point of the co-added images and D the diameter of the aperture used (the current masks use $D = 2$ arcsec). The factor in the square root is the number of pixels in the aperture.

APPENDIX C: PHOTOMETRIC REDSHIFTS RESULTS

We show complementary photometric redshifts results.

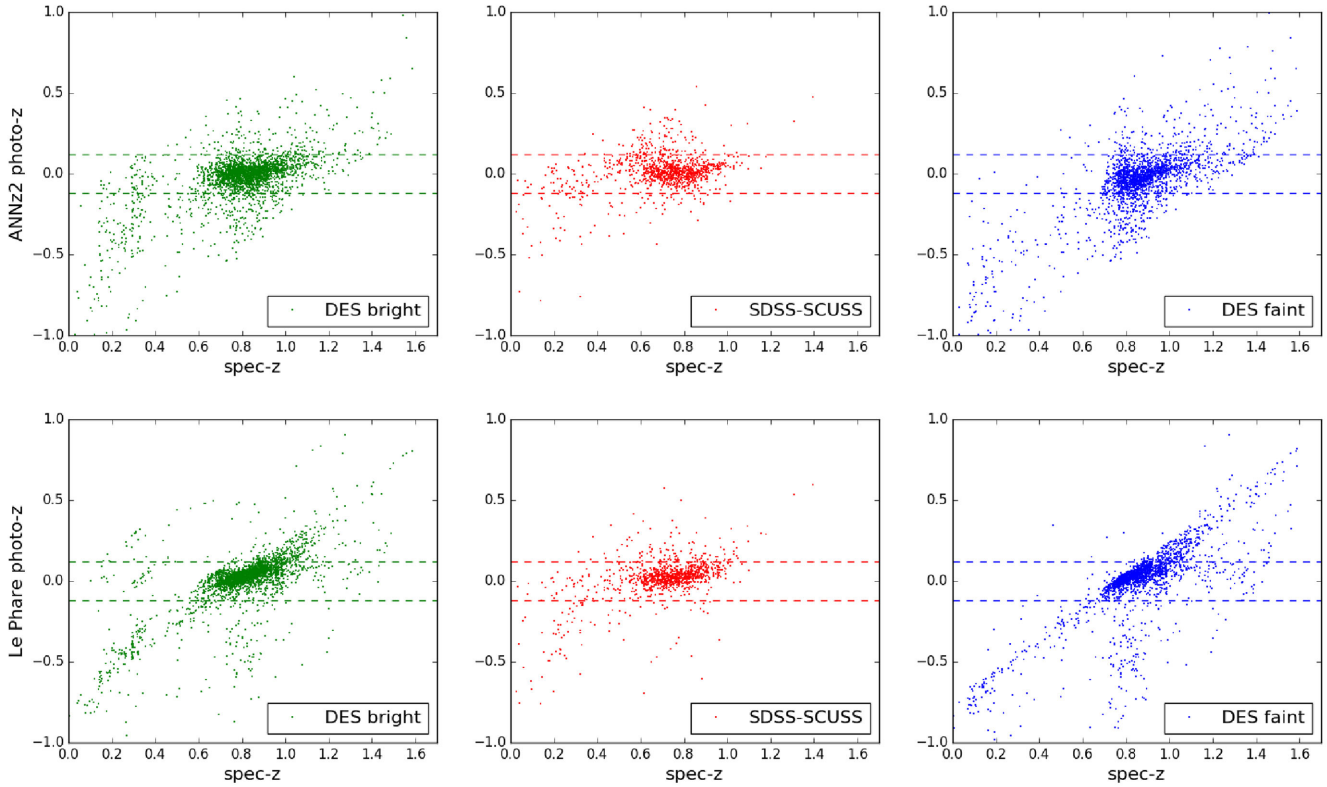

Figure C1. Top and bottom panels show respectively ANNZ2 and LE PHARE photometric redshift results for the three eBOSS spectroscopic samples.

APPENDIX D: EBOSS SYSTEMATICS

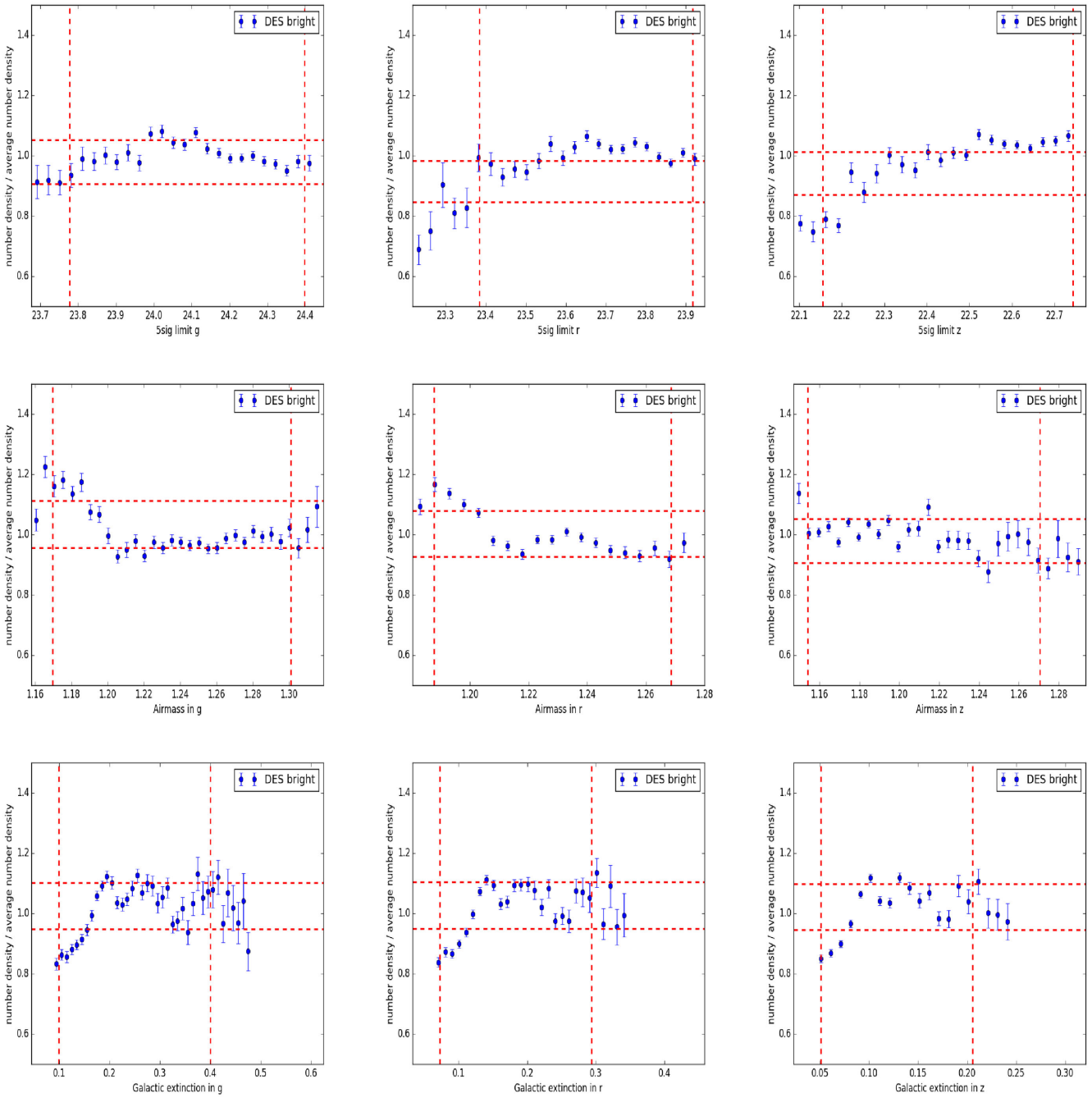

Figure D1. Density fluctuation of galaxies as a function of the depth, airmass and Galactic extinction in the top, middle and bottom row for the *g*,*r*,*z* bands. The two vertical and horizontal red axes show respectively the 5 and 95 per cent of the depth, airmass, galactic extinction distribution and 15 per cent around the mean galaxy density fluctuate ion for the eBOSS target selection.

[1]*Department of Physics and Astronomy, University College London, 132 Hampstead road, London NW1 2PS, UK*
[2]*Laboratoire d'Astrophysique, Ecole polytechnique Federale de Lausanne, CH-1015 Lausanne, Switzerland*
[3]*Instituto de Física Teoŕica, (UAM/CSIC), Universidad Autónoma de Madrid, Cantoblanco, E-28049 Madrid, Spain*
[4]*Departamento de Física Teórica M8, Universidad Autónoma de Madrid (UAM), Cantoblanco, E-28049, Madrid, Spain*
[5]*Departamento de Física Matemática, Instituto de Física, Universidade de São Paulo, São Paulo-SP, CEP 05508-090, Brazil*
[6]*Laboratório Interinstitucional de e-Astronomia-LIneA, Rua Gal. José Cristino 77, Rio de Janeiro RJ-20921-400, Brazil*
[7]*Observatório Nacional, Rua Gal. José Cristino 77, Rio de Janeiro RJ-20921-400, Brazil*
[8]*Department of Physics and Electronics, Rhodes University, PO Box 94, Grahamstown 6140, South Africa*
[9]*Fermi National Accelerator Laboratory, PO Box 500, Batavia, IL 60510, USA*
[10]*Campus of International Excellence UAM+CSIC, Cantoblanco, E-28049 Madrid, Spain*
[11]*Lawrence Berkeley National Laboratory, 1 Cyclotron Road, Berkeley, CA 94720, USA*
[12]*Instituto de Astrofísica de Andalucía (CSIC), Glorieta de la Astronomía, E-18080 Granada, Spain*

[13]*Department of Physics and Astronomy, Johns Hopkins University, 3400 N. Charles Street, Baltimore, MD 21218, USA*
[14]*Instituto de Astronoma, Universidad Nacional Autonoma de Mexico, A.P. 70-264, 04510 Mexico, D.F., Mexico*
[15]*Cerro Tololo Inter-American Observatory, National Optical Astronomy Observatory, Casilla 603, La Serena, Chile*
[16]*Institute of Astronomy, University of Cambridge, Madingley Road, Cambridge CB3 0HA, UK*
[17]*Kavli Institute for Cosmology, University of Cambridge, Madingley Road, Cambridge CB3 0HA, UK*
[18]*CNRS, UMR 7095, Institut d'Astrophysique de Paris, F-75014 Paris, France*
[19]*Sorbonne Universités, UPMC Univ Paris 06, UMR 7095, Institut d'Astrophysique de Paris, F-75014 Paris, France*
[20]*Institute of Cosmology & Gravitation, University of Portsmouth, Portsmouth PO1 3FX, UK*
[21]*Department of Astronomy, University of Illinois, 1002 W. Green Street, Urbana, IL 61801, USA*
[22]*National Center for Supercomputing Applications, 1205 West Clark St., Urbana, IL 61801, USA*
[23]*Institut de Ciències de l'Espai, IEEC-CSIC, Campus UAB, Carrer de Can Magrans, s/n, 08193 Bellaterra, Barcelona, Spain*
[24]*Institut de Física d'Altes Energies, Universitat Autònoma de Barcelona, E-08193 Bellaterra, Barcelona, Spain*
[25]*Kavli Institute for Particle Astrophysics & Cosmology, PO Box 2450, Stanford University, Stanford, CA 94305, USA*
[26]*Excellence Cluster Universe, Boltzmannstr. 2, D-85748 Garching, Germany*
[27]*Faculty of Physics, Ludwig-Maximilians University, Scheinerstr. 1, D-81679 Munich, Germany*
[28]*Department of Physics and Astronomy, University of Pennsylvania, Philadelphia, PA 19104, USA*
[29]*Jet Propulsion Laboratory, California Institute of Technology, 4800 Oak Grove Dr., Pasadena, CA 91109, USA*
[30]*Kavli Institute for Cosmological Physics, University of Chicago, Chicago, IL 60637, USA*
[31]*Department of Physics, University of Michigan, Ann Arbor, MI 48109, USA*
[32]*Max Planck Institute for Extraterrestrial Physics, Giessenbachstrasse, D-85748 Garching, Germany*
[33]*Universitäts-Sternwarte, Fakultät für Physik, Ludwig-Maximilians Universität München, Scheinerstr. 1, D-81679 München, Germany*
[34]*Center for Cosmology and Astro-Particle Physics, The Ohio State University, Columbus, OH 43210, USA*
[35]*Department of Physics, The Ohio State University, Columbus, OH 43210, USA*
[36]*Australian Astronomical Observatory, North Ryde, NSW 2113, Australia*
[37]*George P. and Cynthia Woods Mitchell Institute for Fundamental Physics and Astronomy, and Department of Physics and Astronomy, Texas A&M University, College Station, TX 77843, USA*
[38]*Institució Catalana de Recerca i Estudis Avançats, E-08010 Barcelona, Spain*
[39]*SLAC National Accelerator Laboratory, Menlo Park, CA 94025, USA*
[40]*Department of Physics and Astronomy, Pevensey Building, University of Sussex, Brighton BN1 9QH, UK*
[41]*Centro de Investigaciones Energéticas, Medioambientales y Tecnológicas (CIEMAT), Codigo Postal 28040, Madrid, Spain*
[42]*Instituto de Física, UFRGS, Caixa Postal 15051, Porto Alegre RS-91501-970, Brazil*
[43]*Department of Physics, The Ohio State University, Columbus, OH 43210, USA*
[44]*Department of Physics, University of Illinois, 1110 W. Green St., Urbana, IL 61801, USA*
[45]*Department of Physics and Astronomy, University of Utah, 115 S 1400 E, Salt Lake City, UT 84112, USA*

This paper has been typeset from a TEX/LATEX file prepared by the author.